ARTICLE

https://doi.org/10.1038/s41586-018-0237-5

Nuclear ARP2/3 drives DNA break clustering for homology-directed repair

Benjamin R. Schrank[1], Tomas Aparicio[1], Yinyin Li[2], Wakam Chang[3], Brian T. Chait[2], Gregg G. Gundersen[3], Max E. Gottesman[4] & Jean Gautier[1,5]*

DNA double-strand breaks repaired by non-homologous end joining display limited DNA end-processing and chromosomal mobility. By contrast, double-strand breaks undergoing homology-directed repair exhibit extensive processing and enhanced motion. The molecular basis of this movement is unknown. Here, using *Xenopus laevis* cell-free extracts and mammalian cells, we establish that nuclear actin, WASP, and the actin-nucleating ARP2/3 complex are recruited to damaged chromatin undergoing homology-directed repair. We demonstrate that nuclear actin polymerization is required for the migration of a subset of double-strand breaks into discrete sub-nuclear clusters. Actin-driven movements specifically affect double-strand breaks repaired by homology-directed repair in G2 cell cycle phase; inhibition of actin nucleation impairs DNA end-processing and homology-directed repair. By contrast, ARP2/3 is not enriched at double-strand breaks repaired by non-homologous end joining and does not regulate non-homologous end joining. Our findings establish that nuclear actin-based mobility shapes chromatin organization by generating repair domains that are essential for homology-directed repair in eukaryotic cells.

DNA double-strand breaks (DSBs) induce chromatin movement. In budding yeast, which repair DSBs primarily by homology-directed repair (HDR), induction of a single chromosomal break triggers increased local mobility: the DSB mean-square displacement is substantially higher than that of an undamaged region[1,2]. Moreover, multiple DSBs form clusters after traversing long distances[3]. DSB clustering may facilitate homology search, increase repair efficiency or shield breaks from misrepair[4,5]. These movements are intricately related to HDR. Factors that are critical for initiation of resection and downstream recombination are essential for DSB mobility in yeast[1,2]. In mammalian cells, DSBs are often described as more stable, suggesting that non-homologous end joining (NHEJ), the predominant repair pathway, limits movement[6–8]. However, in human HeLa cells, RAD51-positive DSBs induced by alpha particles form clusters[4]. Similarly, damaged telomeres in human U2OS cells that are maintained by recombination merge in a RAD51-dependent manner[9]. Moreover, damaged active genes cluster in preparation for HDR[5]. Movement of deprotected mouse telomeres requires the LINC (linker of nucleoskeleton and cytoskeleton) complex, which transmits cytoskeletal forces from the cytoplasm to the nucleus[10]. The molecular basis of DSB movement and its role in DNA repair remain unclear.

The machinery that drives actin polymerization in the cytoplasm is also found in the nucleus[11]. Specifically, the ARP2/3 complex and its activator WASP, a Wiskott–Aldrich syndrome (WAS) protein family member, are located in both cellular compartments[12–14]. WASP brings the ARP2 and ARP3 subunits into close proximity to activate the complex and enable filament elongation[15]. Genotoxic agents trigger actin polymerization in the nucleoplasm of mammalian cells[16]; however, the role of actin polymerization in DSB repair has not been characterized.

Actin nucleators bind damaged chromatin

We performed an unbiased proteomics screen to document the recruitment of proteins to chromosomal DSBs in cell-free S-phase extracts derived from *Xenopus* eggs. Peptides from control or DSB-containing chromatin protein fractions were labelled with isobaric tags and subjected to liquid chromatography–mass spectrometry. We observed enrichment of known DSB repair regulators and proteins not previously associated with the DNA damage response (Extended Data Fig. 1a). Among these proteins were all seven subunits of the ARP2/3 complex, as well as β-actin and capping proteins (Extended Data Fig. 1a). We confirmed by western blotting that β-actin, ARPC4, and CAPZβ are recruited to MRE11-enriched, DSB-containing chromatin (Fig. 1a). We next investigated whether actin enrichment at chromosomal DSBs required DNA damage signalling. Inhibition of the phosphatidylinositol-3-OH kinase (PI(3)K)-like kinases ATM and ATR reduced the binding of actin complexes to damaged chromatin (Extended Data Fig. 1b, c). Moreover, treatment with the small molecule inhibitor CK-666, which stabilizes the ARP2/3 complex in an open, inactive conformation[17,18], decreased enrichment of ARPC4, β-actin, and CAPZβ in damaged chromatin (Fig. 1a, b). Overall, these results reveal that PI(3)K-like kinases and the ARP2/3 complex regulate the assembly of polymerized actin at chromosomal DSBs in *Xenopus* extracts.

WASP and ARP2/3 bind DSBs undergoing HDR

We next tested whether WASP localized to DSB foci in mammalian cells. Generation of DSBs by neocarzinostatin (NCS), a radiomimetic antibiotic, induced the formation of WASP foci in U2OS cells (Fig. 2a, b). Moreover, WASP substantially co-localized with γH2AX, which marks large chromatin domains surrounding DSBs[19], suggesting that sites of DNA repair contain WASP (Fig. 2c). Similarly, WASP foci arose in mouse-tail fibroblasts (MTFs) after DSB generation and co-localized with γH2AX (Extended Data Fig. 1d–f).

We next investigated whether actin complexes are recruited in close proximity to DSBs. Accordingly, we performed chromatin immunoprecipitation (ChIP) experiments in U2OS cells in which genome-wide DSBs had been generated by nuclear translocation of the AsiSI

[1]Institute for Cancer Genetics, College of Physicians and Surgeons, Columbia University, New York, NY, USA. [2]Laboratory of Mass Spectrometry and Gaseous Ion Chemistry, The Rockefeller University, New York, NY, USA. [3]Department of Pathology and Cell Biology, College of Physicians and Surgeons, Columbia University, New York, NY, USA. [4]Department of Biochemistry and Biophysics, College of Physicians and Surgeons, Columbia University, New York, NY, USA. [5]Department of Genetics and Development, College of Physicians and Surgeons, Columbia University, New York, NY, USA. *e-mail: jg130@cumc.columbia.edu

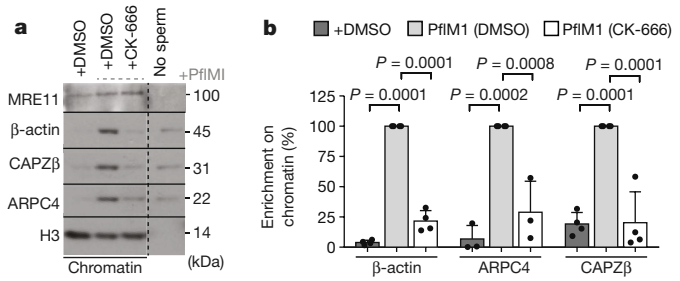

Fig. 1 | Actin complexes are recruited to damaged chromatin. a, Western blot showing enrichment of actin complexes in chromatin damaged using the PflMI restriction endonuclease (+PflMI). MRE11 indicates DNA damage. **b**, Protein quantification in chromatin relative to +PflMI samples. *P* calculated by one-way ANOVA with multiple comparisons; data shown as mean and s.d.; $n = 4$, 3, and 4 independent experiments, left to right.

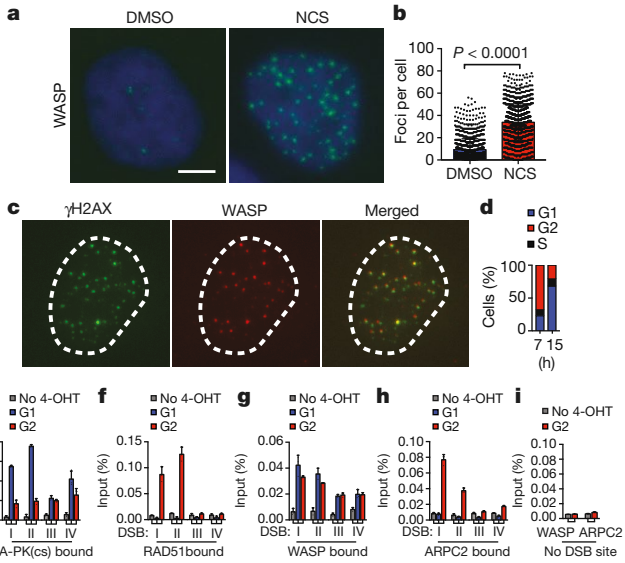

Fig. 2 | ARP2/3 and WASP co-localize at HDR breaks. a, Representative U2OS cells with WASP foci. **b**, Quantification of WASP foci. *P* calculated by two-sided Mann–Whitney test; data shown as mean and s.d.; $n = 1{,}231$ (DMSO), 1,327 nuclei (NCS). **c**, Co-localization of γH2AX with WASP ($n = 30$ nuclei; $r = 0.60 \pm 0.07$, Pearson). **d**, Cell cycle distribution of synchronized ER-AsiSI U2OS cells (U2OS cells stably expressing the AsiSI restriction endonuclease tethered to the oestrogen receptor) after thymidine release. **e**–**h**, ChIP showing enrichment of DNA-PKcs (**e**), RAD51 (**f**), WASP (**g**), and ARPC2 (**h**) at DSBs I–IV in G1 and G2 cells. Mean and s.d. ($n = 3$ technical replicates) of a representative experiment (out of two independent experiments). **i**, Mean and s.d. enrichment of ARPC2 and WASP at an undamaged site in G2 cells ($n = 3$ technical replicates) of a representative experiment (out of two independent experiments). Scale bar, 10 μm.

restriction enzyme[20]. We interrogated four DSB sites, annotated DSBs I–IV, in synchronized cells during the G1 or G2 phase of the cell cycle (Fig. 2d). First, we monitored the recruitment of RAD51 and the catalytic subunit of DNA-dependent protein kinase (DNA-PKcs). RAD51 has been shown to localize to a subset of these DSBs[20]. DNA-PKcs was recruited to all four DSBs in both cell-cycle phases (Fig. 2e). By contrast, RAD51 bound exclusively to DSBs I and II, and this binding was more robust in the G2 phase than in the G1 phase (Fig. 2f). Together, these results demonstrate that HDR can occur at a subset of DSBs in G2 and distinguished from DSBs undergoing NHEJ, the more frequent mode of repair.

We next tested whether actin filament nucleators localize to DSB sites. WASP accumulated at DSBs I and II in both cell cycle phases (Fig. 2g), whereas ARPC2 recruitment was restricted to G2 (Fig. 2h). Notably, WASP was also enriched at DSBs III and IV, whereas ARPC2 was not (Fig. 2g, h). Neither WASP nor ARPC2 were enriched at an undamaged site (Fig. 2i). Collectively, these data establish that WASP binds DSBs independently of repair pathway choice but specifically activates ARP2/3 at DSBs undergoing HDR. This supports a model in which actin polymerization is primed at all DSBs but is triggered only during the assembly of HDR machinery.

ARP2/3 inactivation impairs DSB movement

The ARP2/3 complex generates propulsive forces by nucleating a highly-branched network of actin filaments. As WASP and ARP2/3 localized to RAD51-bound DSBs, we investigated whether their activity induced movement and clustering of HDR machinery. Accordingly, we visualized DSB movements in a U2OS cell line that stably expresses RAD52 tagged with mCherry and 53BP1 tagged with yellow fluorescent protein (YFP)[21]. RAD52 mediates recombination and forms foci exclusively in S/G2 cells[21,22]. Generation of DSBs in S/G2 cells yielded robust induction of RAD52–mCherry foci (Fig. 3a). Strikingly, RAD52 foci clustered and merged over a 60-min interval (Fig. 3a, b and Supplementary Video 1a–d). Coalescing foci increased in intensity and size and remained merged for a minimum of 15 min (Fig. 3b, c). Notably, inactivation of ARP2/3 using CK-666 decreased the frequency of clustering events and prevented the increase in the size of foci (Fig. 3c, d and Supplementary Video 1e, f). We subsequently compared DSB movements in the presence of CK-666 with those in the presence of CK-689, an inactive control analogue[18]. Quantitative analysis of DSB tracks in CK-689-treated cells indicated that RAD52 foci explored a mean cumulative distance of 4.1 μm over 100 min (Fig. 3e, f). Mean-square displacement (MSD) analysis of Rad52 foci revealed a diffusion coefficient $D(t)$ of $3.7 \times 10^{-5}\,\mu m^2\,s^{-1}$ (Fig. 3g and Extended Data Fig. 2a). Motion type analysis was consistent with confined Brownian motion. Critically, inhibition of ARP2/3 diminished the distance travelled by DSBs over the 100-min period (Fig. 3e, f). Furthermore, CK-666 treatment decreased the RAD52 diffusion coefficient from $3.7 \times 10^{-5}\,\mu m^2\,s^{-1}$ to $1.8 \times 10^{-5}\,\mu m^2\,s^{-1}$ (Fig. 3g).

We subsequently monitored DSBs bound by replication protein A (RPA) in MTFs expressing RPA32 tagged with enhanced GFP and a nuclear localization sequence (RPA32–pEGFP–NLS). Similar to the behaviour of RAD52–mCherry foci, RPA32 foci frequently merged over a 60-min interval (Fig. 3h and Supplementary Video 1g, h). Notably, CK-666 treatment diminished the distance travelled by RPA foci relative to CK-689 treatment (Fig. 3i). Moreover, the diffusion coefficient calculated for RPA foci in cells treated with CK-666 decreased from $4.1 \times 10^{-5}\,\mu m^2\,s^{-1}$ (for cells treated with CK-689) to $2.1 \times 10^{-5}\,\mu m^2\,s^{-1}$ (Extended Data Fig. 2a). Finally, we used MTFs harbouring a conditional *Arpc2* allele[23]. Upon 4-OHT treatment, these cells are depleted of ARPC2[23] (Fig. 3j). Consistent with CK-666-treated cells, RPA movements were significantly attenuated in ARCP2-depleted cells (Fig. 3i–l). CK-689 affected RAD52 and RPA foci movement only minimally relative to DMSO (Extended Data Fig. 2a, b).

The formation of Rad51 filaments requires single-stranded DNA (ssDNA)–RPA intermediates. Thus, we assessed how ARP2/3 inactivation affected the behaviour of RAD51 foci. To circumvent the lack of a functional fluorescent RAD51 reporter, we used Icy bioimaging software and its spatial analysis plug-in (http://www.icy.bioimage analysis.org) to assess clustering of RAD51 foci. This approach was validated in a study showing ATM-dependent clustering of γH2AX foci in fixed cells[24]. Analysis with Icy software revealed that RAD51 foci were highly clustered in the nucleus and that CK-666 reduced this clustering (Extended Data Fig. 3a–d). CK-666 treatment did not affect cell viability, cell cycle progression, nuclear size, nuclear morphology, or the expression of RPA or RAD51 (Extended Data Fig. 4a–g). These experiments demonstrate that ARP2/3-mediated actin polymerization enhances DSB motion during HDR, thereby increasing the clustering of foci.

During the G1 phase of the cell cycle, 53BP1 forms foci and regulates end-joining events. Consistent with the lack of ARP2/3 at DSBs

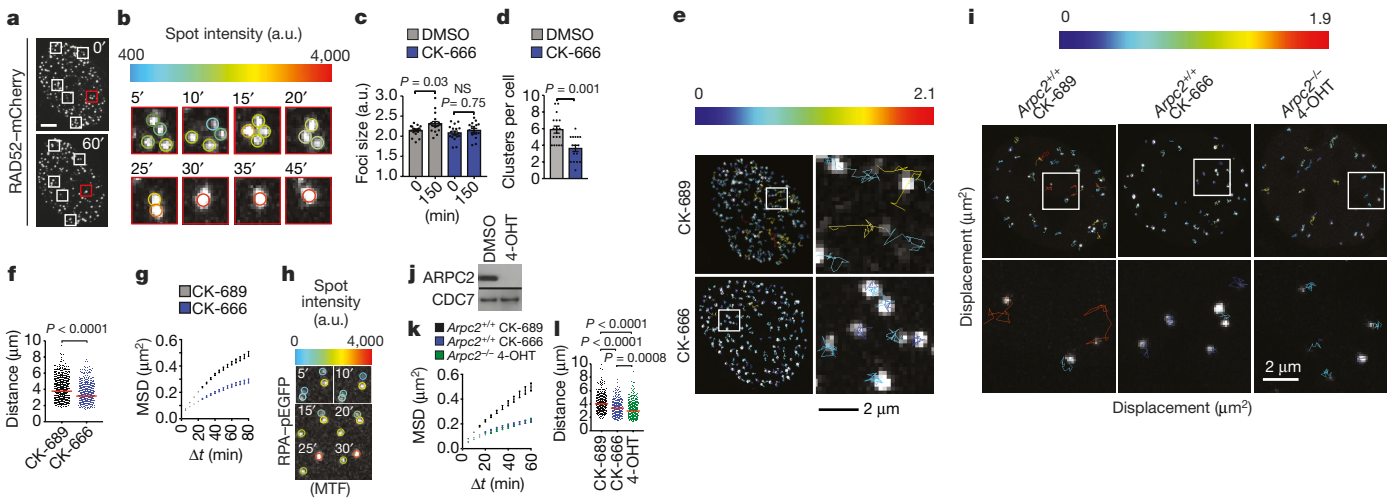

Fig. 3 | Arp2/3 drives DSB mobility during HDR. a, A representative U2OS cell nucleus with boxes indicating clustering of RAD52–mCherry foci. **b**, Expanded images of clustering from **a** (red box). Circles denote intensity of foci. **c**, Size of RAD52 foci (*P* calculated by one-way ANOVA with multiple comparisons; data shown as mean and s.e.m.; $n = 19$ nuclei (DMSO), 17 nuclei (CK-666). **d**, RAD52–mCherry clustering events (*P* calculated by two-tailed Mann–Whitney test; data shown as mean and s.e.m.; $n = 17$ nuclei (DMSO), 16 nuclei (CK-666). **e**, Traces of RAD52–mCherry foci over 100 min. Expanded images of boxed tracks (right). **f**, Median cumulative distance travelled by RAD52–mCherry foci. *P* calculated by two-tailed Mann–Whitney test; $n = 1{,}120$ foci from 13 nuclei (CK-689), 720 foci from 12 nuclei (CK-666). **g**, MSD of RAD52–mCherry foci. Data shown as mean and weighted s.e.m.; $n = 3{,}262$ foci from 13 nuclei (CK-689), 2,143 foci from 12 nuclei (CK-666). Δt, time interval. **h**, Clustering of pEGFP–RPA32–NLS foci in MTFs. **i**, Traces of RPA32–pEGFP–NLS foci over 100 min. **j**, ARPC2 protein levels in whole-cell lysates from Arpc2-LoxP-CreER MTFs (single experiment). **k**, MSD of RPA32–pEGFP–NLS foci. Data shown as mean and weighted s.e.m.; $n = 790$ foci from 13 nuclei (CK-689), 823 foci from 12 nuclei (CK-666), 1,135 foci from 13 nuclei (4-OHT). Scale bars, 5 μm or as indicated. **l**, Median cumulative distance travelled by RPA32–pEGFP–NLS foci. *P* calculated by one-way ANOVA with multiple comparisons; $n = 381$ foci from 13 nuclei (CK-689), 370 foci from 12 nuclei (CK-666), 425 from 13 nuclei (4-OHT).

in G1 cells (Fig. 2), the movement of 53BP1–YFP foci in G1 cells was unaffected by ARP2/3 inhibition (Extended Data Figs. 2a, 5a–c). In G2 cells, many 53BP1–YFP and RAD52 foci colocalized, consistent with the localization of 53BP1 at sites of DSB resection[22] (Extended Data Fig. 5d). The diffusion coefficient for 53BP1 foci increased from $2.4 \times 10^{-5}\,\mu m^2\,s^{-1}$ in G1 cells to $3.5 \times 10^{-5}\,\mu m^2\,s^{-1}$ in G2 cells (Extended Data Fig. 5e, f). Unlike in G1 cells, the motion of 53BP1 foci in G2 cells was reduced by ARP2/3 inactivation (Extended Data Fig. 5g). Collectively, these data indicate that ARP2/3 enhances the motion of sites of DSB resection in G2 cells.

ARP2/3 nucleates actin foci at sites of HDR

Genotoxic agents induce nuclear actin structures in mammalian cells[16]. In U2OS cells transfected with nuclear actin-chromobody TagGFP[25], we identified a subset of actin structures resembling foci (actin-cb foci); the number of these foci increased after NCS treatment (Fig. 4a, b and Extended Data Fig. 6a, b). We also identified brighter, rod-like filaments (Extended Data Fig. 6a, b). Strikingly, actin-cb foci clustered and merged over a 20-min interval (Fig. 4c and Supplementary Video 2a, b). MSD analysis of actin-cb foci revealed a $D(t)$ of $3.4 \times 10^{-4}\,\mu m^2\,s^{-1}$ (Fig. 4d, e). Similar to RAD52 and RPA, the α-coefficient for actin-cb

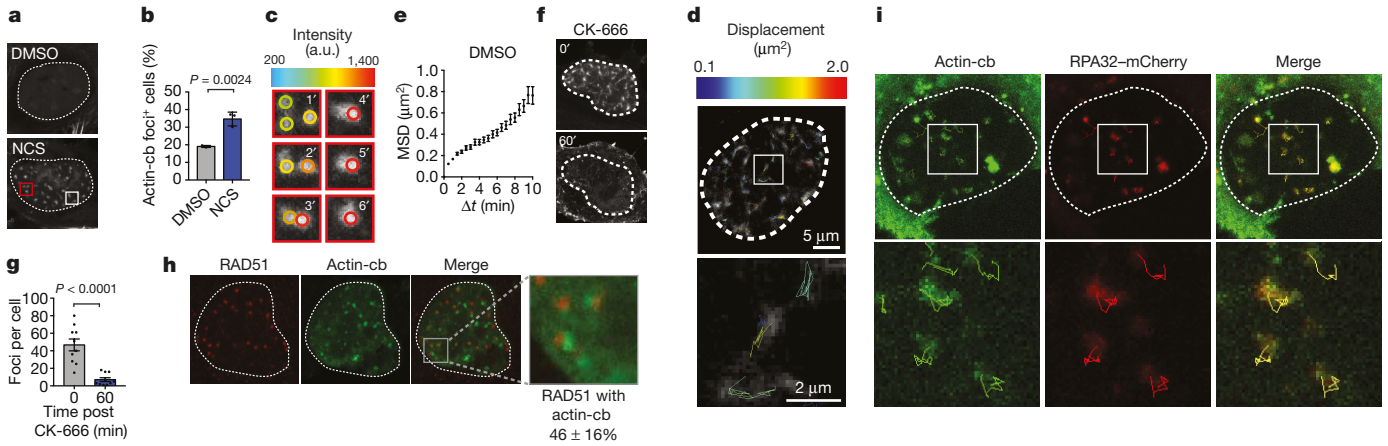

Fig. 4 | Nuclear actin foci cluster and localize to HDR sites. **a**, Representative images of U2OS nuclei transfected with nuclear actin-chromobody TagGFP. Boxes indicate clustering events. **b**, Percentage of cells with actin-cb foci from 3 biological replicates. *P* calculated by Student's two-tailed *t*-test; data shown as mean and s.d.; $n = 473$ nuclei (DMSO), 473 nuclei (NCS). **c**, Expanded images of a clustering event from **a** (red box). Circles denote intensity of foci. **d**, Representative traces of actin-cb foci (out of three independent experiments) over 10 min. **e**, MSD of actin-cb foci. Data shown as mean and weighted s.e.m.; DMSO $n = 662$ foci from 11 nuclei. **f**, Representative images of a U2OS nucleus with actin-cb foci following CK-666 treatment. **g**, Quantification of actin-cb foci before and after CK-666 treatment. *P* calculated by paired two-tailed *t*-test; data shown as mean and s.e.m.; $n = 10$ nuclei from two independent experiments. **h**, Representative images of a U2OS nucleus showing RAD51 co-localization with actin-cb foci. The percentage of RAD51 foci that overlap or touch actin-cb foci is shown ($n = 12$ nuclei). **i**, Representative images of a U2OS nucleus (from five independent experiments) showing traces of RPA32–mCherry–NLS foci (red) and actin-cb foci (green). Scale bars, 5 μm or as indicated.

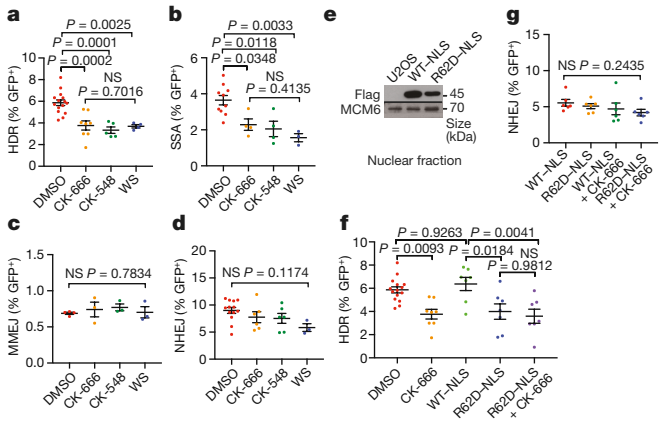

Fig. 5 | WASP and ARP2/3 mediate HDR. a, Summary of DR-GFP assay, which monitors recombination between two GFP repeats ($n = 15, 7, 5, 4$ left to right). NS, not significant. **b**, Summary of SA-GFP (SSA) assay ($n = 10, 4, 4, 3$ left to right). **c**, Summary of EJ2-GFP (MMEJ) assay ($n = 4, 3, 3, 3$, left to right). **d**, Summary of EJ5-GFP (NHEJ) assay ($n = 13, 6, 6, 3$, left to right). **e**, Western blot shows Flag-WT-NLS or Flag-R62D-NLS overexpression in U2OS nuclear soluble fraction (single experiment). **f**, DR-GFP assay in cells transfected with Flag-WT-NLS or Flag-R62D-NLS. ($n = 7, 7, 7$, left to right). HDR efficiency in the presence of DMSO or CK-666 (Fig. 5a) shown for comparison. **g**, EJ5-GFP assay in cells transfected with Flag-WT-NLS or Flag-R62D-NLS. ($n = 6, 6, 6$, left to right). For **a**–**g**, *P* calculated by one-way ANOVA with multiple comparisons as indicated; data shown as mean and s.e.m. *n* represents independent experiments. WS, Wiskostatin.

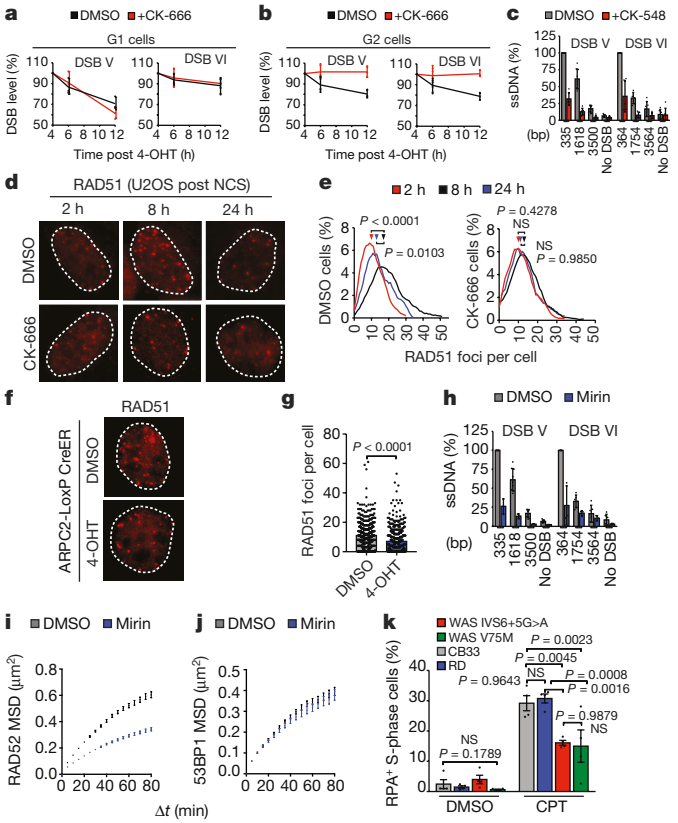

Fig. 6 | ARP2/3 facilitates resection and repair in G2. a, DSB repair at DSBs V and VI in G1-synchronized, ER-AsiSI-AID U2OS cells (tagged with an auxin-inducible degron (AID) that ablates the enzyme upon auxin treatment). Mean and s.d. ($n = 3$ technical replicates) of a representative experiment shown. **b**, DSB repair at DSBs V and VI in G2-synchronized ER-AsiSI-AID U2OS cells. Mean and s.d. ($n = 3$ technical replicates) of a representative experiment shown. **c**, Enrichment of ssDNA at DSBs V and VI following CK-548 treatment. Data shown as mean and s.d., $n = 6$ replicates from two independent experiments. **d**, Representative images of U2OS nuclei showing RAD51 foci. **e**, Quantification of RAD51 foci. *P* calculated by one-way ANOVA with multiple comparisons; smoothed traces show distribution of RAD51 foci. Arrows above curves indicate mean number of foci per cell. DMSO: 2 h $n = 1,830$ cells, 8 h $n = 2,440$ cells, 24 h $n = 782$ cells; CK-666: 2 h $n = 2,438$ cells, 8 h $n = 2,189$ cells, 24 h $n = 912$ cells. **f**, Representative images of ARPC2-LoxP-CreER MTF nuclei showing RAD51 foci. **g**, Quantification of RAD51 foci in MTFs. *P* calculated by two-tailed Mann–Whitney test; data shown as mean; $n = 571$ nuclei (DMSO), 462 nuclei (4-OHT). **h**, Representative ssDNA enrichment at DSBs V and VI following mirin treatment. Data shown as mean and s.d.; $n = 3$ replicates of two independent experiments. ssDNA in DMSO-treated cells (Fig. 5c) shown for comparison. **i**, MSD of RAD52–mCherry foci. Data shown as mean and weighted s.e.m.; DMSO $n = 3,292$ foci from 12 cells, mirin $n = 2,677$ foci from 11 cells. **j**, MSD of 53BP1–YFP foci in G1 cells. Data shown as mean and weighted s.e.m.; DMSO $n = 893$ foci from 12 cells, mirin $n = 744$ foci from 14 cells. **k**, Quantification of chromatin-bound RPA in S-phase cells. *P* calculated by two-way ANOVA with multiple comparisons; data shown as mean and s.e.m.; $n = 4$ independent experiments. WAS IVS6+5G>A and WAS V75M are cells carrying WAS mutations. RD and CB33, healthy lymphocytes. All DMSO columns, not significant ($P = 0.1789$). For CPT, CB33 versus RD, not significant ($P = 0.9643$); WAS IVS6+5G>A versus WAS V75M, not significant ($P = 0.9879$); CB33 versus WAS IVS6+5G>A, $P = 0.0045$; CB33 versus WAS V75M, $P = 0.0023$; RD versus WAS IVS6+5G>A, $P = 0.0016$; RD versus WAS V75M, $P = 0.0008$.

foci indicated confined motion. Notably, CK-666 abolished actin-cb foci, strongly suggesting that these structures are sites of ARP2/3-dependent nucleation (Fig. 4f, g, Supplementary Video 2c–e and Extended Data Fig. 6d). By contrast, nuclear actin rods exhibited limited mobility and were unaffected by CK-666 (Extended Data Fig. 6a–d). Finally, we compared the localization of actin-cb foci with RAD51 foci in fixed cells and RPA32–mCherry foci using live cell imaging. Following NCS treatment, 46% of RAD51 foci overlapped or abutted actin-cb foci (Fig. 4h). Moreover, we observed co-localization of actin-cb foci and RPA32–mCherry foci, which travelled together in the nucleoplasm (Fig. 4i and Extended Data Fig. 6e, f). Collectively, these experiments provide direct evidence that ARP2/3 assembles dynamic nuclear actin structures at sites of HDR.

WASP and ARP2/3 mediate HDR but not NHEJ

To determine how DSB clustering affects DNA repair pathways, we used a panel of U2OS cell lines to monitor the repair of DSBs induced by the bacterial endonuclease I-SceI by HDR, NHEJ, single-strand annealing (SSA), and microhomology-mediated end joining (MMEJ)[26]. Inactivation of ARP2/3 by CK-666 or CK-548 reduced the ability of cells to repair I-SceI-induced DSBs using HDR or SSA by 40% (Fig. 5a, b and Extended Data Fig. 7a, e). Similarly, wiskostatin, a small-molecule inhibitor of WASP[27], reduced the efficiency of HDR and SSA (Fig. 5a, b). Cells depleted of WASP by RNA interference showed similar defects in HDR (Extended Data Fig. 7b–d). Notably, inhibition of WASP or ARP2/3 did not compromise MMEJ or NHEJ, neither of which require substantial resection (Fig. 5c, d and Extended Data Fig. 7f, g). Finally, the application of CK-689 did not reduce the repair of I-SceI-induced DSBs by HDR, SSA or NHEJ (Extended Data Fig. 7h).

Although the ARP2/3 complex is found in the nucleus[14], it also polymerizes actin in the cytoplasm. To support the idea that the HDR defect was a direct consequence of inhibiting nuclear actin polymerization, we increased nuclear actin levels by overexpressing actin fused to a nuclear localization sequence (actin–NLS) (Fig. 5e). Whereas expression of wild-type actin–NLS did not affect HDR, overexpression of an actin variant that interrupts filament formation (actin(R62D)–NLS) inhibited HDR to levels comparable with ARP2/3 inhibition (Fig. 5f). Treatment of cells expressing actin(R62D)–NLS with CK-666 did not further reduce HDR, suggesting that nuclear actin and ARP2/3 functioned together. Moreover, expression of wild-type actin, actin(R62D), or wild-type actin–NLS tagged with mCherry did not affect DSB repair, whereas expression of actin(R62D)–NLS significantly inhibited HDR (Extended Data Fig. 8a, b). This strongly suggests that inhibition of

actin polymerization in the cytoplasm does not influence DNA repair in the nucleus. Similar to CK-666, expression of actin(R62D)–NLS did not reduce NHEJ-based repair (Fig. 5g). Finally, neither small interfering RNA (siRNA) directed against the actin filament nucleator formin-2 nor treatment with the formin inhibitor SMIFH2 inhibited HDR efficiency (Extended Data Fig. 8c–f). This observation demonstrates a specific requirement for ARP2/3 complex activity in HDR.

ARP2/3 activity enhances DSB resection

To assess the functional importance of ARP2/3-driven DSB mobility, we compared the repair kinetics of two AsiSI-induced DSB sites (DSBs V and VI) that undergo up to 3.5 kb of resection[28]. In G1 cells, the repair kinetics of both DSBs were identical in the presence or absence of CK-666, confirming that ARP2/3 does not influence NHEJ (Fig. 6a). By contrast, in G2 cells, CK-666 substantially slowed repair at these DSB sites (Fig. 6b).

To investigate how actin-driven clustering might promote HDR efficiency, we tested whether the ARP2/3 complex facilitates resection. Inactivation of the ARP2/3 complex decreased ssDNA generation at DSBs V and VI by 50%, indicating that clustering facilitates DSB end-resection (Fig. 6c). We consolidated this finding by quantifying RAD51 foci that arose following DSB resection in NCS-treated cells over 24 h (Fig. 6d, e). In control cells, the number of RAD51 foci first increased between 2 and 8 h and then decreased up to 24 h, indicative of recruitment and repair (Fig. 6d). By contrast, RAD51 foci increased minimally following ARP2/3 inhibition (Fig. 6d, e). Moreover, substantially fewer RAD51 foci arose in ARPC2-depleted MTFs than in control MTFs (Fig. 6f, g).

In yeast and human cells, DSB motion requires the HDR machinery[1,2,5]. We wondered whether RAD52 movement requires the activity of the MRN (MRE11, RAD50 and NBS1) complex[29]. Accordingly, we treated U2OS cells with mirin, a small-molecule inhibitor that abolishes the nuclease activity of MRE11[30]. Mirin lowered ssDNA levels at DSBs V and VI by 70% (Fig. 6h). Notably, mirin substantially decreased the $D(t)$ of RAD52 foci from $4.4 \times 10^{-5}\,\mu m^2\,s^{-1}$ to $2.4 \times 10^{-5}\,\mu m^2\,s^{-1}$ (Fig. 6i and Extended Data Fig. 2a), but did not significantly affect the MSD of 53BP1 foci in G1 cells (Fig. 6j). Together, these observations suggest a positive feedback loop, wherein resection enhances DSB movements, which, in turn, enhance resection.

WAS is an X-linked disorder characterized by severe immunodeficiency and predisposition to non-Hodgkin's lymphoma and leukaemia[31]. Given that inactivation of WASP by wiskostatin or siRNA produced defects in HDR (Fig. 5a and Extended Data Fig. 7d), we tested B lymphocytes derived from patients with WAS for defects in DSB end-resection. Relative to lymphocytes derived from healthy individuals, lymphocytes bearing two distinct WAS mutations exhibited 50% fewer RPA-positive cells upon exposure to the DNA topoisomerase I inhibitor camptothecin (CPT), consistent with a resection defect (Fig. 6k and Extended Data Fig. 9a–d). Moreover, WAS mutant cells were more sensitive to CPT treatment than healthy lymphocytes (Extended Data Fig. 10a, b). Inhibition of ARP2/3 by CK-666 also enhanced CPT-induced lethality in U2OS cells (Extended Data Fig. 10c). Finally, inhibition of ARP2/3 sensitized cells to the DNA polymerase inhibitor aphidicolin and the PARP1 inhibitor olaparib, indicating a reduced tolerance to replication stress (Extended Data Fig. 10d, e). Together, these results demonstrate that activation of ARP2/3 by WASP enhances the processing and resolution of DSBs undergoing HDR.

Discussion

DSB mobility is influenced by cell cycle stage, chromatin state, and repair pathway choice. Our finding that ARP2/3 specifically enhances the movement of breaks undergoing HDR is supported by studies showing that DSB mobility requires DNA end-resection. DSBs induced in pericentric heterochromatin during the S and G2 phases of the cell cycle relocate to the nuclear periphery, whereas DSBs generated during the G1 phase remain stable[32]. Critically, blocking HDR or resection prevented DSB mobility in G2. Similarly, in *Drosophila*, the activities of CtIP, Exo1, and Blm were necessary for DSB movement outside the heterochromatic domain[33]. Notably, DSBs within heterochromatin in *Drosophila* relocalize to repair sites along nuclear actin filaments in an ARP2/3-dependent process[34]. Conversely, we now show that inhibition of ARP2/3 decreases end- processing, consistent with positive feedback regulation between DSB mobility and resection. Indeed, DSB clustering could facilitate enzymatic reactions by increasing the local concentration of repair factors. Notably, in budding yeast, Arp2, Arp3, and Arpc2 are synthetic lethal in combination with Mre11 or Sgs1 deficiency[35]. This supports interdependency of actin polymerization and resection.

Our ChIP analyses suggest a two-step mechanism for actin nucleation at HDR sites (Extended Data Fig. 10f). WASP is recruited at all DSBs regardless of cell cycle stage, reminiscent of NHEJ factors. By contrast, ARP2/3 is recruited in G2 to breaks that assemble HDR machinery. Actin polymerization promoted by WASP and ARP2/3 might therefore require sequential activation of PI(3)K-like kinases. Whereas ATM promotes the assembly of complexes required for resection, ATR commits repair to HDR[29]. Accordingly, following ATM activation and WASP recruitment at DSBs, resection initiation could create a permissive environment for ARP2/3 activity leading to increased chromosomal mobility at specific DSB sites.

Online content

Any Methods, including any statements of data availability and Nature Research reporting summaries, along with any additional references and Source Data files, are available in the online version of the paper at https://doi.org/10.1038/s41586-018-0237-5.

Received: 5 October 2017; Accepted: 17 April 2018;
Published online: 20 June 2018

1. Dion, V., Kalck, V., Horigome, C., Towbin, B. D. & Gasser, S. M. Increased mobility of double-strand breaks requires Mec1, Rad9 and the homologous recombination machinery. *Nat. Cell Biol.* **14**, 502–509 (2012).
2. Miné-Hattab, J. & Rothstein, R. Increased chromosome mobility facilitates homology search during recombination. *Nat. Cell Biol.* **14**, 510–517 (2012).
3. Lisby, M., Mortensen, U. H. & Rothstein, R. Colocalization of multiple DNA double-strand breaks at a single Rad52 repair centre. *Nat. Cell Biol.* **5**, 572–577 (2003).
4. Aten, J. A. et al. Dynamics of DNA double-strand breaks revealed by clustering of damaged chromosome domains. *Science* **303**, 92–95 (2004).
5. Aymard, F. et al. Genome-wide mapping of long-range contacts unveils clustering of DNA double-strand breaks at damaged active genes. *Nat. Struct. Mol. Biol.* **24**, 353–361 (2017).
6. Lemaître, C. et al. Nuclear position dictates DNA repair pathway choice. *Genes Dev.* **28**, 2450–2463 (2014).
7. Robinett, C. C. et al. *In vivo* localization of DNA sequences and visualization of large-scale chromatin organization using lac operator/repressor recognition. *J. Cell Biol.* **135**, 1685–1700 (1996).
8. Soutoglou, E. et al. Positional stability of single double-strand breaks in mammalian cells. *Nat. Cell Biol.* **9**, 675–682 (2007).
9. Cho, N. W., Dilley, R. L., Lampson, M. A. & Greenberg, R. A. Interchromosomal homology searches drive directional ALT telomere movement and synapsis. *Cell* **159**, 108–121 (2014).
10. Lottersberger, F., Karssemeijer, R. A., Dimitrova, N. & de Lange, T. 53BP1 and the LINC complex promote microtubule-dependent DSB mobility and DNA repair. *Cell* **163**, 880–893 (2015).
11. Virtanen, J. A. & Vartiainen, M. K. Diverse functions for different forms of nuclear actin. *Curr. Opin. Cell Biol.* **46**, 33–38 (2017).
12. Taylor, M. D. et al. Nuclear role of WASp in the pathogenesis of dysregulated TH1 immunity in human Wiskott–Aldrich syndrome. *Sci. Transl. Med.* **2**, 37ra44 (2010).
13. Wu, X. et al. Regulation of RNA-polymerase-II-dependent transcription by N-WASP and its nuclear-binding partners. *Nat. Cell Biol.* **8**, 756–763 (2006).
14. Yoo, Y., Wu, X. & Guan, J. L. A novel role of the actin-nucleating Arp2/3 complex in the regulation of RNA polymerase II-dependent transcription. *J. Biol. Chem.* **282**, 7616–7623 (2007).
15. Pollard, T. D. & Borisy, G. G. Cellular motility driven by assembly and disassembly of actin filaments. *Cell* **112**, 453–465 (2003).
16. Belin, B. J., Lee, T. & Mullins, R. D. DNA damage induces nuclear actin filament assembly by Formin-2 and Spire-1/2 that promotes efficient DNA repair. *eLife* **4**, e07735 (2015).
17. Hetrick, B., Han, M. S., Helgeson, L. A. & Nolen, B. J. Small molecules CK-666 and CK-869 inhibit actin-related protein 2/3 complex by blocking an activating conformational change. *Chem. Biol.* **20**, 701–712 (2013).
18. Nolen, B. J. et al. Characterization of two classes of small molecule inhibitors of Arp2/3 complex. *Nature* **460**, 1031–1034 (2009).

19. Rogakou, E. P., Boon, C., Redon, C. & Bonner, W. M. Megabase chromatin domains involved in DNA double-strand breaks *in vivo*. *J. Cell Biol*. **146**, 905–916 (1999).
20. Aymard, F. et al. Transcriptionally active chromatin recruits homologous recombination at DNA double-strand breaks. *Nat. Struct. Mol. Biol*. **21**, 366–374 (2014).
21. Karanam, K., Kafri, R., Loewer, A. & Lahav, G. Quantitative live cell imaging reveals a gradual shift between DNA repair mechanisms and a maximal use of HR in mid S phase. *Mol. Cell* **47**, 320–329 (2012).
22. Ochs, F. et al. 53BP1 fosters fidelity of homology-directed DNA repair. *Nat. Struct. Mol. Biol*. **23**, 714–721 (2016).
23. Rotty, J. D. et al. Profilin-1 serves as a gatekeeper for actin assembly by Arp2/3-dependent and -independent pathways. *Dev. Cell* **32**, 54–67 (2015).
24. Caron, P. et al. Non-redundant functions of ATM and DNA-PKcs in response to DNA double-strand breaks. *Cell Rep*. **13**, 1598–1609 (2015).
25. Plessner, M., Melak, M., Chinchilla, P., Baarlink, C. & Grosse, R. Nuclear F-actin formation and reorganization upon cell spreading. *J. Biol. Chem*. **290**, 11209–11216 (2015).
26. Gunn, A. & Stark, J. M. I-SceI-based assays to examine distinct repair outcomes of mammalian chromosomal double strand breaks. *Methods Mol. Biol*. **920**, 379–391 (2012).
27. Peterson, J. R. et al. Chemical inhibition of N-WASP by stabilization of a native autoinhibited conformation. *Nat. Struct. Mol. Biol*. **11**, 747–755 (2004).
28. Zhou, Y., Caron, P., Legube, G. & Paull, T. T. Quantitation of DNA double-strand break resection intermediates in human cells. *Nucleic Acids Res*. **42**, e19, doi:10.1093/nar/gkt1309 (2014).
29. Symington, L. S. & Gautier, J. Double-strand break end resection and repair pathway choice. *Annu. Rev. Genet*. **45**, 247–271 (2011).
30. Dupré, A. et al. A forward chemical genetic screen reveals an inhibitor of the Mre11-Rad50-Nbs1 complex. *Nat. Chem. Biol*. **4**, 119–125 (2008).
31. Massaad, M. J., Ramesh, N. & Geha, R. S. Wiskott-Aldrich syndrome: a comprehensive review. *Ann. NY Acad. Sci*. **1285**, 26–43 (2013).
32. Tsouroula, K. et al. Temporal and spatial uncoupling of DNA double strand break repair pathways within mammalian heterochromatin. *Mol. Cell* **63**, 293–305 (2016).
33. Chiolo, I. et al. Double-strand breaks in heterochromatin move outside of a dynamic HP1a domain to complete recombinational repair. *Cell* **144**, 732–744 (2011).
34. Caridi, C. P. et al. Nuclear F-actin and myosins drive relocalization of heterochromatic breaks. *Nature* https://doi.org/10.1038/s41586-018-0242-8 (2018).
35. van Pel, D. M., Stirling, P. C., Minaker, S. W., Sipahimalani, P. & Hieter, P. *Saccharomyces cerevisiae* genetics predicts candidate therapeutic genetic interactions at the mammalian replication fork. *G3* **3**, 273–282 (2013).

Acknowledgements We thank T. Swayne and E. L. Munteanu from the Confocal and Specialized Microscopy Shared Resource of the Irving Cancer Research Center (ICRC) and the Flow Cytometry Shared Resource of the ICRC at Columbia University (supported by NIH grants #P30-CA013696, #S10-RR025686); J. Stark for the GFP reporter cell lines; G. Legube for the ER-AsiSI U2OS lines and for sharing unpublished data; J. Bear for the ARPC2-LOXP-CreER MTFs; G. Lahav for the RAD52–mCherry U2OS line; R. Dalla-Favera for the RD and CB33 cell lines; J. Lukas for the pEGFP–NLS–RPA32 construct; R. Baer for the I-SceI plasmid; N. Kato and T. Lagache for manuscript comments; and A. Hollar for Metacyte classifier design. This work was supported by the NIH (R35-CA197606 and P01-CA174653 to J.G., RO1-GM099481 to G.G.G., PHS-GM103314 and PHS-GM109824 to B.T.C., and F30-CA217049 to B.R.S.).

Author contributions J.G. and B.R.S conceived the study and wrote the manuscript. B.R.S. conducted the majority of the experiments and data analyses. T.A. and Y.L. performed the mass spectrometry experiments. G.G.G., M.E.G., W.C., B.T.C., T.A. and Y.L. assisted with data analysis and interpretation.

Competing interests The authors declare no competing interests.

Additional information
Extended data is available for this paper at https://doi.org/10.1038/s41586-018-0237-5.
Supplementary information is available for this paper at https://doi.org/10.1038/s41586-018-0237-5.
Reprints and permissions information is available at http://www.nature.com/reprints.
Correspondence and requests for materials should be addressed to J.G.
Publisher's note: Springer Nature remains neutral with regard to jurisdictional claims in published maps and institutional affiliations.

METHODS

Chromatin binding assay and western blot. Preparation of low-speed supernatant (LSS) *Xenopus* egg extracts and isolation of demembranated sperm nuclei (chromatin) were performed as previously described[36]. For chromatin binding experiments, 15 μl LSS extract was supplemented with demembranated sperm nuclei (2,500 sperm per μl) and incubated for 10 min at 21 °C before addition of DMSO or one of the following compounds for 10 min: CK-666 (160 μM), CK-548 (160 μM), KU55933 (100 μM), VE821 (50 μM). Subsequently, the PflMI restriction endonuclease was added to each sample (0.05 U/μl) before incubation for an additional 60 min at 21 °C. Extracts were diluted in chromatin isolation buffer (50 mM HEPES-KOH, pH 7.8, 100 mM KCl, 2.5 mM $MgCl_2$) supplemented with 0.125% Triton X-100 and overlaid on top of sucrose cushions (chromatin isolation buffer plus 30% sucrose) in 1.5-ml low-retention tubes (Thermo Fisher Scientific). Samples were spun at 7,180 r.p.m. for 30 min at 4 °C in a swing-bucket Sorval rotor (HB-6). Chromatin pellets were resuspended in 10 μl Laemmli buffer, boiled, and fractionated on a 4–22% Tris-glycine gel (Invitrogen) according to standard procedures, followed by transfer of resolved proteins onto PVDF membranes. Following a 1-h block with 5% milk, membranes were incubated overnight at 4 °C with one of the following primary antibodies: β-actin (Sigma Aldrich: A5316, 1/1,000), ARPC4 (Novus Biologicals: NBP1-69003, 1/500), capping protein β-2 subunit (Developmental Studies Hybridoma Bank: E00007, 1/10,000), histone H3 (Cell Signaling Technology, 9715, 1/2,000) and *Xenopus* Mre11[36]. HRP-conjugated secondary antibodies were used (anti-rabbit IgG HRP, anti-mouse IgG HRP, Fisher Scientific) and chemiluminescence (Supersignal West Pico Chemiluminescent Substrate, 34077) was used.

Mass spectrometric analysis of DSB-containing chromatin. Chromatin samples were isolated as described above with the following modifications: 100 μl LSS extract was supplemented with sperm nuclei (5,000 sperm per μl) and incubated for 10 min at 21 °C before addition of PflMI restriction endonuclease (0.05 U/μl) and incubated for an additional 60 min. Chromatin was isolated through sucrose cushions as described above and extensively digested with 100 U micrococcal nuclease for 30 min at 37 °C (NEB). Chromatin proteins were reduced with dithiothreitol (5 mM, 30 min 60 °C) and alkylated with iodoacetamide (15 mM, 30 min, room temperature) before fractionation on SDS–PAGE. 'In-gel' digestion was performed with proteomic-grade trypsin (Promega) at 5 ng/μl for 16 h at 37 °C. The resulting digestion peptides were extracted from the gel pieces with 1:2 (vol:vol) 5% formic acid: acetonitrile solution. The resulting peptides were labelled with isobaric mass tags (ITRAQ 4-plex, Sciex), combined, purified with in-house made STAGE tips[37], resuspended in 0.5% acetic acid and loaded onto a home-packed reverse phase C18 column (75 μm ID). The peptides were separated using a linear gradient (0–42% acetonitrile, 0.5% acetic acid, 120 min, 150 nl/min) and directly sprayed into an LTQ-Orbitrap-Velos mass spectrometer for analysis (Thermo). The repetitive analytical cycle incorporated a high-resolution mass scan in the Orbitrap (resolution 30,000) followed by tandem MS scans of the five most intense peaks observed in each Orbitrap mass spectrum. Peptides were identified and quantified using Proteome Discoverer software (Thermo, Version 1.4).

Cell culture and drug treatment. U2OS and mouse-tail fibroblast cell lines were cultured in high-glucose Dulbecco's modified Eagle's medium supplemented with L-glutamine, 10% fetal bovine serum, and 1% penicillin-streptomycin. For neocarzinostatin-dependent DSB induction, cells were cultured on 8-well chamber slides (Thermo Fisher Scientific) and were treated with 0.5 μg/ml NCS for 60 min at 37 °C. Cells were washed twice with PBS before the addition of medium containing DMSO or one of the following compounds: CK-666 (Sigma Aldrich: SML-006, 100 μM), CK-548 (Sigma Aldrich: C7499, 50 μM), CK-689 (Sigma Aldrich: 18251750, 100 μM), and wiskostatin (Sigma Aldrich: W2270, 3 μM). After drug treatment, cells were then incubated at 37 °C for the indicated times. For mirin experiments, cells were pre-treated with mirin (Sigma Aldrich: M9948, 50 μM) for 1 h, before addition of NCS.

ER-AsiSI U2OS cells stably expressing the AsiSI restriction endonuclease tethered to the oestrogen receptor were provided by G. Legube (Centre de Biologie Integrative, Toulouse). For cell synchronization, cells were treated with 2 mM thymidine for two 18-h intervals separated by an 11-h release in fresh medium. Cells underwent double-thymidine block and were released into fresh medium for 7 h (G2) or 15 h (G1) before AsiSI-dependent DSB induction with medium supplemented with 300 nM 4-OHT (Sigma Aldrich, H7904) plus CK-666, CK-548, wiskostatin, or DMSO. Cells were subsequently incubated at 37 °C for 4 h.

Arpc2$^{-/-}$ fibroblast cell lines (provided by J. E. Bear, University of North Carolina) stably express the Cre-recombinase tagged to the oestrogen receptor. Upon 4-OHT treatment, the *Arpc2* locus is floxed by Cre and cells are depleted of ARPC2 following 4 days of 4-OHT treatment.

CB33 and RD lymphoblastoid B cell lines were a gift from R. Dalla-Favera (Columbia University). Two B lymphocyte cell lines bearing distinct mutations in the *WAS* gene were obtained from the NIGMS Human Genetic Cell Repository (Coriell: GM1267, GM1268). GM1267 harbours a G>A transition at position 4 in intron 6 of the *WAS* gene (IVS6+5G>A). This mutation activates a cryptic splice site leading to splicing of a 38-nucleotide sequence from intron 6 onto exon 7. GM1268 harbours a G>A transition at nucleotide 257 in exon 2 on the WAS gene. This mutation results in a methionine-for-valine substitution at codon 75 (V75M). All B cell lines were grown in Rosewell Park Memorial Institute medium with 20% heat-inactivated bovine serum with 2 mM L-glutamine added. All cell lines were tested for mycoplasma contamination.

Immunohistochemistry and quantification of DSB repair protein foci. U2OS cells were cultured on 8-well chamber slides (Thermo Fisher Scientific) and subjected to drug treatments as described above. Cells were then washed once with PBS before fixation with freshly prepared 4% PFA (pH 7.4) for 10 min. Cells were subsequently washed twice with PBS for 10 min before permeabilization with 0.1% PBS-Triton X-100 for 10 min. Cells were then washed once with PBS for 5 min before incubation with blocking buffer (3% BSA in 0.2% PBS-Tween) for 1 h. Cells were stained with primary antibodies diluted in blocking buffer under a Hybrislip (Invitrogen) overnight in a humidified chamber at 4 °C. Primary antibodies include γH2AX (EMD Millipore: 05-636, 1/500 or Abcam: ab81299, 1/500), WASP (Santa Cruz: sc-5300, 1/50), RAD51 (Santa Cruz: sc-8349, 1/50), 53BP1 (Novus Biologicals: NC100-304, 1/250) and Flag (Sigma Aldrich: F3165, 1/250). Cells were then washed three times in PBS for 15 min and incubated with a fluorescence-conjugated secondary antibody in PBS with DAPI (Invitrogen, 1/10,000) for 1 h at room temperature. Secondary antibodies were Alexa 488 conjugated goat anti-mouse Ig (Abcam: ab150113, 1/1,000), Alexa 488 conjugated goat anti-rabbit Ig (Thermo Fisher Scientific, A-11034, 1/10,000), and Alexa 594 conjugated goat anti-mouse Ig (Thermo Fisher Scientific, A-11005, 1/10,000). Cells were then washed three times with PBS for 15 min. Vectashield was applied to each slide and slides were coverslipped. Slides were analysed under 40× magnification using a Zeiss Axio Imager Z2 microscope, equipped with a CoolCube1 camera (Carl Zeiss). Images were processed for contrast enhancement and background reduction using ImageJ.

MetaCyte software (Metasystems, version 3.10.6) was used to detect U2OS nuclei based on DAPI staining and to perform automated quantification of γH2AX, RAD51, and WASP foci within each nucleus. For analysis of the size and clustering of foci, images were converted to greyscale and processed with Icy Software (Version 1.8.6.0; Institut Pasteur, Quantitative Image Analysis Unit; http://www.icy.bioimageanalysis.org). Regions of interest were drawn around individual nuclei and foci were detected using the Spot Detector plug-in (Channel 0)[38]. For clustering analyses, spots detected using Scale 2 (3 pixels) were exported to the spatial analysis plug-in, which uses Ripley's *K* function to assess the deviance of pairs of points from total randomness[24,38]. The software reports statistically significant clustering ($P < 0.05$) when the *K* function crosses the clustering threshold. The software further corrects for the number of points in the computations of the quantiles of the Ripley's *K* function. Thus, there is no loss of statistical power for samples with lower numbers of foci. For foci size analysis, foci with minimum sizes of 1 and 3 pixels were counted using the Spot Detector plug-in. Scale 1 was used to detect foci that were at least 1 pixel in size, whereas Scale 2 was used to detect foci that were at least 3 pixels. Foci that met criteria for both Scale 1 and Scale 2 were excluded from the Scale 1 group to avoid duplicate detections. Foci counts were subsequently averaged to determine the mean size of foci per nucleus (100 nuclei were detected per condition or as indicated). For co-localization studies, images were imported into Image J (NIH) and separated into green (γH2AX) and red (WASP) channels. These files were subsequently imported into Icy and regions of interest were drawn around individual nuclei. Pearson's *r* was calculated using the Co-localization Studio plug-in, which compares the coincidence of spots inside a region of interest between green and red channels.

Chromatin immunoprecipitation. ChIP experiments followed previously published protocols[20] with the following modifications: 50 million ER-AsiSI U2OS cells were cultured on 150-mm^2 plates in high-glucose Dulbecco's modified Eagle's medium supplemented with L-glutamine, 10% fetal bovine serum, and 1% penicillin-streptomycin. Following double-thymidine block, cells were released into fresh medium for 7 h (G2) or 15 h (G1) before incubation with 300 nM 4-OHT for 4 h. Cells were then trypsinized, washed with PBS, cross-linked in 1% methanol-free formaldehyde fixing buffer for 10 min, quenched with 0.125 M glycine for 5 min, and snap frozen at −80 °C. Cell lysis and nuclear isolation were performed using NP40 lysis buffer and SDS shearing buffer (Covaris). Nuclei were sonicated using the S220 Ultrasonicator (Covaris) to obtain chromatin fragments of 500–1,000 bp in length. Sheared chromatin was incubated with 10 μg antibodies to RAD51 (Santa Cruz: sc-8349), DNA-PKcs (Abcam: ab1832), WASP (Santa Cruz: sc-5300), ARPC2 (Santa Cruz: sc-32195) or IgG (Jackson ImmunoResearch Laboratories) overnight. These antibodies were validated for ChIP by previous studies[12,20]. Protein A/G magnetic beads were added overnight, followed by sequential washes at increasing stringency and reverse cross-linking at 65 °C. Immunoprecipitated DNA and input DNA were analysed in triplicate

by qPCR. ChIP efficiencies (measured as per cent of input immunoprecipitated) were measured by qPCR at sites 80 bp downstream of DSBs. Graphs show ChIP efficiencies in G1, G2, or no 4-OHT cells, pooled from three experiments, and normalized against input material. Sequences for primers are listed below: DSB I: 5′-GTCCCTCGAAGGGAGCAC-3′, 5′-CCGACTTTGCTGTGTGACC-3′; DSB II: 5′-CCGCCAGAAAGTTTCCTAGA-3′, 5′-CTCACCCTTGCAGCACTTG-3′; DSB III: 5′-TCCCCTGTTTCTCAGCACTT-3′, 5′- CTTCTGCTGTTCTGCGTCCT-3′; DSB IV: 5′-ATCGGGCCAATCTCAGAGG-3′, 5′-GCGACGCTAACGTTA AAGCA-3′. Primer pairs used to measure RAD51, DNA-PKcs, WASP, and ARPC2 were located 80 bp from DSB sites or at an undamaged genomic locus.

I-SceI-induced DSB repair assays. U2OS cell lines which harbour chromosomally integrated I-SceI-based GFP reporter substrates were used to monitor the efficiency of HDR, SSA, MMEJ, and c-NHEJ repair processes. The DR-GFP, SA-GFP, EJ2-GFP, and EJ5-GFP cell lines (gifts from J. Stark, City of Hope Cancer Center) were transfected with 1 μg I-SceI-expressing vector (FuGENE 6 transfection reagent (Promega), Opti-MEM (Gibco)) in medium supplemented with DMSO or one of the following compounds: CK-666 (Sigma Aldrich: SML-006, 50 μM), CK-548 (Sigma Aldrich: C7499, 25 μM), CK-689 (Sigma Aldrich: 182517, 50 μM), SMIFH2 (Sigma Aldrich: S4826, 5 μM), or wiskostatin (Sigma Aldrich: W2270, 3 μM). The I-SceI-expressing vector was a gift from R. Baer. For the Flag actin construct overexpression experiments, DR-GFP cells were transfected with Flag–actin–NLS or Flag–actin(R62D)–NLS for 48 h before transfection with I-SceI in medium supplemented with DMSO or CK-666. For the mCherry actin construct overexpression experiments, DR-GFP cells were co-transfected with I-SceI and mCherry–actin, mCherry–actin–NLS, mCherry–actin(R62D), or mCherry– actin(R62D)–NLS. Cells were harvested 48 h after I-SceI transfection and percentage GFP^+ events were counted by fluorescence-activated cell sorting (FACS) (10,000 cells per biological replicate). For all conditions, parallel transfection with 1 μg pEGFP-N3 vector (Clontech) was used to determine transfection efficiency. Percentage refers to the number of GFP^+ cells divided by the number of $pEGFP^+$ cells.

Resection assay. A detailed protocol for the resection assay has been recently described[28]. In brief, ER-AsiSI U2OS cells were treated with 300 nM 4-OHT in medium supplemented with DMSO, CK-548 (50 μM), or CK-666 (100 μM). For mirin experiments, cells were pre-treated with mirin (Sigma Aldrich: M9948, 50 μM) for 1 h before addition of 4-OHT, and subsequently washed and incubated with mirin for the indicated times. After 4 h, cells were trypsinized and washed with cold PBS before resuspension in lysis buffer (100 mM NaCl, 10 mM TrisCl pH 8, 25 mM EDTA, pH 8, 0.5% SDS, 0.1 mg/ml proteinase K). Cells were agitated at 37 °C overnight. After phenol/chloroform purification and salt/ethanol extraction, precipitated DNA underwent restriction enzyme digestion by BamHI-HF, BsrGI, or HindIII-HF (1 unit enzyme per 7 ng DNA) at 37 °C overnight. DNA digests were subsequently used as templates in a 20 μl qPCR reaction containing 10.0 μl 2× TaqMan Universal PCR Master mix (Thermo), 0.5 μM of each primer, and 0.2 μM of probe. The extent of ssDNA generation at sites downstream of various DSBs was determined by calculating the ΔCt value for each site (mock-digested Ct value − digest Ct value) and using the following equation: $\text{ssDNA} = 1/(2^{(\Delta Ct - 1) + 0.5)} \times 100$. Sequences for primers and probes are listed below: DSB V (335 bp site): 5′-GAATCGGATGTATGCGACTGATC-3′, 5′-TTCCAAAGTTATTCCAACCCGAT-3′; 6FAM-CACAGCTTGCCCATCCT TGCAAACC-TAMRA; DSB V (1618 bp site): 5′- TGAGGAGGTGACATTAGAA CTCAGA-3′, 5′-AGGACTCACTTACACGGCCTTT-3′; 6FAM-TTGCAAGG CTGCTTCCTTACCATTCAA-TAMRA; DSB V (3500 bp site): 5′-TCCTAGCCAG ATAATAATAGCTATACAAACA-3′, 5′-TGAATAGACAGACAACAGATAAA TGAGACA-3′; 6FAM-ACCCTGATCAGCCTTTCCATGGGTTAAG-TAMRA; DSB VI (364 bp site): 5′-CCAGCAGTAAAGGGGAGACAGA-3′, 5′-CTGTTCAATCGTCTGCCCTTC-3′; 6FAM-CCAGGCCCTCAAAATC CCTCCACTG-TAMRA; DSB VI (1754 bp site): 5′- GAAGCCATCCTACTCTTC TCACCT-3′, 5′-GCTGGAGATGATGAAGCCCA-3′; 6FAM-CACTCCCTGTTC TTCTTCTGCTCCCGA-TAMRA; DSB VI (3564 bp site): 5′-GCCC AGCTAAGATCTTCCTTCA-3′, 5′-CTCCTTTGCCCTGAGAAGTGA-3′; 6FAM-CTGCAGCCCTCAAGCCCGGAT-TAMRA. No DSB site: 5′- ATTG GGTATCTGCGTCTAGTGAGG-3′, 5′-GACTCAATTACATCCCTGCAGCT-3′; 6FAM-TCTCTGCACAGACCGGCTTCCCTTC-TAMRA.

AsiSI-AID repair assay. The repair assay followed recently published protocols with the following modifications[20,28]. Five million ER-AsiSI-AID U2OS cells were cultured on 100-mm^2 plates in high-glucose Dulbecco's modified Eagle's medium supplemented with L-glutamine, 10% fetal bovine serum, and 1% penicillin-streptomycin. Following double-thymidine block, cells were released into fresh medium for 7 h (G2) or 15 h (G1) before incubation with 300 nM 4-OHT and DMSO or CK-666 (100 μM) for 4 h. Cells were subsequently washed three times with PBS and then incubated in medium containing auxin (Sigma: I5148, 500 μg/ml) and DMSO or CK-666. Cells were harvested 0, 2, or 8 h after auxin exposure. Phenol/chloroform purification followed by salt/ethanol extraction was performed to precipitate DNA. DNA were subsequently used as templates in a 20-μl qPCR reaction containing 10.0 μl 2× TaqMan Universal PCR Master mix (Thermo), 0.5 μM of each primer, and 0.2 μM of probe. The level of unrepaired DSBs was determined by normalizing the Ct value for each DSB site with a control, undamaged site. Sequences for primers and probes are listed below. DSB V (across DSB): 5′-GATGTGGCCAGGGATTGG-3′, 5′-CACTCAAGCCCAACCCGT-3′; DSB VI (across DSB): 5′- GAGGAGCCTCTCCTGCAGC-3′, 5′-GAACCAGACCTAC CTCCAGGG-3′.

Live cell imaging. U2OS cells stably expressing RAD52–mCherry, 53BP1–YFP, and Geminin–CFP constructs[21] were cultured on 35-mm glass bottom microwell dishes (MatTek, P35GC-1.5-10-C). Cells were treated with 0.5 μg/ml NCS to induce DSBs for 60 min at 37 °C. Subsequently, cells were washed twice with PBS before the addition of medium containing DMSO, CK-689 (100 μM), or CK-666 (100 μM). For mirin experiments, cells were pre-treated with mirin (Sigma Aldrich: M9948, 50 μM) for 1 h before addition of NCS, and subsequently washed and incubated with mirin for the indicated times. S-phase cells were selected for RAD52 foci analysis by screening for Geminin–CFP positivity. G1 cells were selected for 53BP1 foci analysis by screening for Geminin–CFP^-/RAD52–$mCherry^-$ cells. After 20 h, images were acquired on an A1RMP confocal microscope (Nikon Instruments), on a TiE Eclipse stand equipped with a 60×/1.49 Apo-TIRF oil-immersion objective lens, an automated XY stage, stage-mounted piezoelectric focus drive, and a heated, humidified stagetop chamber with 5% CO_2 atmosphere. Cells expressing RAD52–mCherry and 53BP1–YFP foci were imaged in GaAsP detectors using 561 nm and 488 nm excitation, respectively, and standard RFP and GFP emission filters. The confocal pinhole was set to 1 Airy unit for the red channel. Foci movements were examined by collecting *z* series at 0.4-μm intervals throughout the entire nucleus every 5 min for 2.5 h. Focus was maintained by the Perfect Focus System (Nikon).

Nuclear actin-chromobody TagGFP imaging and analysis. For live cell imaging experiments, U2OS cells were cultured on 35-mm glass bottom microwell dishes at 90% confluency (MatTek, P35GC-1.5-10-C) and transfected with 0.3 μg of vector expressing nuclear actin-cb (Chromotek, acg-n; EMD Millipore, FuGENE 6 transfection reagent; Promega) After 6 h, cells were treated with 1 μg/ml NCS for 60 min at 37 °C. Cells were washed twice with PBS before the addition of medium containing DMSO. After 3 h, images were acquired on an A1RMP confocal microscope using the equipment and settings described above. Cells with actin-cb foci were classified using the following criteria: actin-cb foci exhibited movement and frequent turnover, were round in morphology and often appeared to have fuzzy 'tails'. Cells with actin-cb rods were classified using the following criteria: actin-cb rods exhibited limited movement, no turnover, were very bright, and were filamentous in morphology. Foci movements were examined by collecting *z* series at 0.4-μm intervals throughout the entire nucleus every 30 s for 10 min. Following initial image acquisition, cells were subsequently treated with 100 μM CK-666. Images of actin-cb foci were subsequently acquired 1 h post CK-666 treatment. Actin-cb foci were scored as the number of discrete punctate structures appearing per nucleus, as detected by the Icy Spot Detector plug-in. For experiments assessing localization of actin-cb foci with RPA, U2OS cells were co-transfected with actin-cb and RPA32–NLS–mCherry (a gift from J. Lukas) for 16 h before NCS treatment. After 12 h, foci movements were examined by collecting *z* series at 0.4-μm intervals throughout the entire nucleus every 5 min for 2.5 h.

For experiments in fixed cells, U2OS cells were cultured on 8-well chamber slides (Thermo Fisher Scientific), subjected to transfection and drug treatments as described above, and processed for IHC as described above. Cells were stained with primary antibodies against RAD51 (Santa Cruz: sc-8349, 1/50) and GFP (Abcam: ab13970, 1/100) overnight. Secondary antibodies were Alexa 488 conjugated goat anti-chicken Ig (Invitrogen: A11039, 1/1000) and Alexa 594 conjugated goat anti-mouse Ig (Thermo Fisher Scientific, A-11005, 1/10000). Actin-cb-expressing cells were selected for analysis by screening for actin-cb foci. Images were acquired on an A1RMP confocal microscope equipped with a 60×/1.49 Apo-TIRF oil-immersion objective lens. *Z* series at 0.4-μm intervals throughout the entire nucleus were acquired. For co-localization analysis, actin-cb and Rad51 foci were detected in *z* using the spot detector plug-in available on Icy Bioimaging Software platform. The co-localization of RAD51 and actin-cb spots was assessed using the Co-localization Studio plug-in, object-based methodology. Here, co-localization was defined as the number of RAD51 spots that directly overlapped with or touched actin-cb foci (within a 0.7-μm radius).

Analysis of movement of DSB foci. DSB movement analysis followed the approach recently described[9]. Nikon NIS Elements data files were processed in ImageJ[39]. Green and red channels were split and a maximum-intensity projection of each *z* stack was generated. T stacks were subsequently aligned using the StackReg plugin[40] to correct for cell movements over the duration of the experiment. Cells that underwent large-scale nuclear deformations or expansions were discarded. The TrackMate plug in for ImageJ[41] was used to perform single-particle tracking of DSB foci over a 100-min interval and monitor foci intensity. Focus trajectories were subsequently exported to MATLAB and analysed using the class @msdanalyzer[42]. The MSD of DNA damage foci plots the average squared distance

travelled by foci at increasing time intervals, whereas the diffusion coefficient $D(t)$ is approximated through the linear-weighted fit of the initial mean MSD curve[42]. MSD curves for DSB foci in a given cell were computed using the formula $\mathrm{MSD} = (x(t+\Delta t) - x(t))^2$, where x reflects focus position and t is the time in minutes. For RAD52 foci, the weighted mean of all the MSD curves acquired from >2,000 tracks in three independent experiments is shown. The error bars for each point on the weighted mean of the MSD curve represent the weighted s.e.m. over all MSD curves. The diffusion coefficient $D(t)$ was estimated from the linear fit of the first 20% of each MSD curve. Calculation of the time-dependence coefficient α was performed using MATLAB via log–log fitting of the power law $\mathrm{MSD}(t) = \Gamma \times t^{\alpha}$. Cumulative distance (CD) was calculated by summing the distances foci travelled over 100 min relative to their starting position using the formula: $D(i) = \sqrt{(X(i) - X(i-1))^2 + (Y(i) - Y(i-1))^2}$ where X and Y refer to the x and y coordinates of the focus at time i.

Analysis of clustering of DSB foci. For analysis of clustering of DSB foci during live cell imaging, a clustering event was defined as complete co-localization of ≥2 foci over ≥3 consecutive frames (15 min) over a 100-min interval. For actin-cb clustering during live cell imaging, a clustering event was defined as complete co-localization of ≥2 foci over ≥3 consecutive frames (3 min) over a 20-min interval.

Quantification of RPA association to chromatin by flow cytometry. Detection of chromatin-bound RPA in S-phase cells followed recently published protocols with the following modifications: 2×10^6 cells were treated with DMSO or 1 μg/ml CPT for 24 h. Cells were subsequently washed once with cold PBS, then incubated in cold CSK buffer + 1% Triton-X for 5 min. Cells were then washed with PBS and fixed in 0.5% PFA for 15 min. Cells were subsequently washed twice in BD Perm/Wash buffer (Becton Dickinson: BD554723) and stained with RPA2/RPA32 antibody (Abcam: ab2175, 1/50) overnight. Cells were then washed with PBS and incubated in secondary antibody (Abcam: ab150113, 1/50 or Alexa 647 conjugated donkey anti-mouse Ig, Invitrogen: A31571, 1/50) for 1 h. Cells were then washed and stained with propidium iodide (PI) in the presence of RNase A overnight. The percentage of S-phase cells as identified by PI staining was quantified by flow cytometry. The gate for RPA-positive cells was established using a negative control sample that was stained with mouse IgG following extraction. RPA-positive cells following DMSO and CPT treatment were subsequently quantified by flow cytometry. A minimum of 10,000 cells was counted per biological replicate.

Clonogenic and cell survival assays. U2OS cells were seeded onto 10-cm dishes (1,000 cells per dish) overnight. Cells were subsequently treated with 0, 100, 200, or 300 μM CK-666 in the presence of DMSO, CPT (10 nM), or aphidocolin (APH, 400 nM) for 12 h. Cells were then washed with PBS and incubated in fresh medium for 10–14 days. Cells were subsequently washed with PBS, fixed for 10 min with 100% methanol, and stained with 0.1% crystal violet for 10 min. For olaparib studies, cells were treated with 0, 10, or 20 μM CK-666 in the presence of DMSO or 50 nM olaparib for 14 days, and fixed and stained as above. Each experiment was performed in triplicate.

For colony quantification, images of dishes were converted to greyscale and processed with Icy Software (Version 1.8.6.0; Institut Pasteur, Quantitative Image Analysis Unit; http://www.icy.bioimageanalysis.org). Regions of interest were drawn around individual dishes and colonies were counted using the Spot Detector plug-in (Channel 0). Counts from two biological replicates were normalized for plating efficiency.

For the annexin V/PI survival assay, $1–5 \times 10^5$ cells were incubated in DMSO or 1 μg/ml CPT for 0, 12, or 24 h. Cells were then washed in 1× binding buffer (Thermo Fisher Scientific: 00-0055) and stained with APC-conjugated annexin V (Thermo Fisher Scientific: 17-8007) for 10 min. Cells were then washed in 1× binding buffer and stained in PI (Thermo Fisher Scientific: 00-6990). Per cent viability following CPT treatment was assessed by measuring the percentage of APC-Annexin V-negative and PI-negative cells by flow cytometry. A minimum of 10,000 cells counted per condition.

Quantification and statistical analysis. Statistical parameters are reported in the figures and legends. Two-tailed t-tests and ordinary one-way ANOVAs were used for comparisons of means of normally distributed data and two-tailed Mann–Whitney U tests were used for comparison of non-normally distributed data. Statistical analyses were performed using Prism 7.0. No statistical methods were used to predetermine sample size. The experiments were not randomized and the investigators were not blinded to allocation during experiments and outcome assessment.

Research animals. The use of *Xenopus laevis* (African clawed frog) in this research proposal was approved (protocol AAAK0551) by the Institutional Animal Care and Use Committee (IACUC) of Columbia University Medical School. All procedures comply with Public Health Service's policies for the humane care and use of laboratory animals.

Reporting summary. Further information on experimental design is available in the Nature Research Reporting Summary linked to this paper.

Data availability. The data that support the findings of this study are available from the corresponding author upon reasonable request. The authors declare that the data supporting the findings of this study are available within the paper and its Supplementary Information files.

36. Peterson, S. E. et al. Cdk1 uncouples CtIP-dependent resection and Rad51 filament formation during M-phase double-strand break repair. *J. Cell Biol.* **194**, 705–720 (2011).
37. Rappsilber, J., Ishihama, Y. & Mann, M. Stop and go extraction tips for matrix-assisted laser desorption/ionization, nanoelectrospray, and LC/MS sample pretreatment in proteomics. *Anal. Chem.* **75**, 663–670 (2003).
38. Lagache, T., Lang, G., Sauvonnet, N. & Olivo-Marin, J. C. Analysis of the spatial organization of molecules with robust statistics. *PLoS ONE* **8**, e80914 (2013).
39. Schindelin, J. et al. Fiji: an open-source platform for biological-image analysis. *Nat. Methods* **9**, 676–682 (2012).
40. Thevenaz, P., Ruttimann, U. E. & Unser, M. A pyramid approach to subpixel registration based on intensity. *IEEE Trans Image Process* **7**, 27–41 (1998).
41. Tinevez, J. Y. et al. TrackMate: An open and extensible platform for single-particle tracking. *Methods* **115**, 80–90 (2017).
42. Tarantino, N. et al. TNF and IL-1 exhibit distinct ubiquitin requirements for inducing NEMO-IKK supramolecular structures. *J. Cell Biol.* **204**, 231–245 (2014).

a

Accession#	Name	Enrichment	Spectral counts
gi148228066	XRCC6	2.1	35
gi148232630	ARPC5	1.8	2
gi148238173	CAPZA1	1.8	8
gi213623693	NBS1	1.6	3
gi122936374	ACTB	1.6	12
gi148231189	ARPC2	1.6	12
gi147903611	ARPC1A	1.6	13
gi119352593	ARPC3	1.5	10
gi119352603	ACTR3	1.4	17
gi119352601	ARPC4	1.3	15
gi119352591	ACTR2	1.1	7

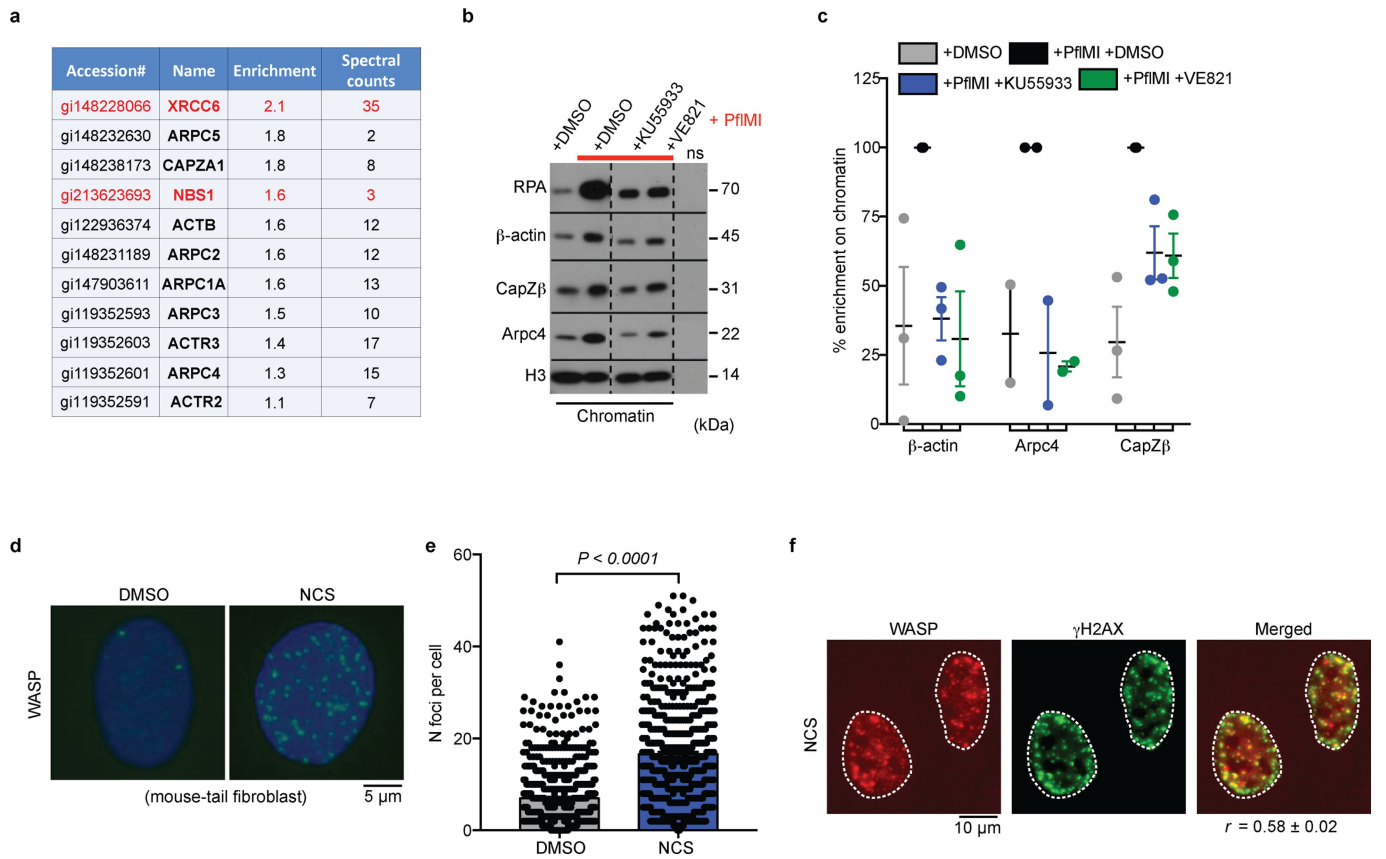

Extended Data Fig. 1 | Actin filament nucleators localize to chromosomal DSBs in *Xenopus* extracts and mammalian cells. **a**, Enrichment ratios and spectral counts of actin complexes and repair proteins in DSB-containing chromatin are shown by liquid chromatography–mass spectrometry. **b**, DNA damage-dependent enrichment of actin complexes (+PflMI) following PIKK inhibition (KU55933: ATMi; VE821: ATRi). RPA shown as a marker of DNA damage. **c**, Quantification of actin complexes in chromatin relative to +PflMI samples. β-actin $n = 3$ independent experiments, ARPC4 $n = 2$ independent experiments, CAPZβ $n = 3$ independent experiments. Mean and s.e.m shown. **d**, Representative images of WASP foci after NCS treatment in MTFs. **e**, Quantification of WASP foci (P calculated by two-sided Mann–Whitney test; data shown as mean; DMSO $n = 578$ nuclei, NCS $n = 556$ nuclei). **f**, Co-localization of γH2AX with WASP foci in MTFs. $n = 22$ nuclei, $r = 0.58 \pm 0.021$, Pearson. Scale bar, 5 μm or as indicated.

a

	Treatment	No cells analyzed (No foci)	Cumulative Distance ± SD (μm)	Diffusion coefficient (10^{-5} μm ^{2}/s)	Anomalous Diffusion Coefficient ± SE	No of experiments
Rad52-mCherry, U2OS (100 min)	DMSO	12 (3292)	4.2 ± 1.29	4.38	0.719 ± 0.006	3
	CK-689 (100 μM)	13 (3262)	3.8 ± 1.08	3.65	0.726 ± 0.006	3
	CK-666 (100 μM)	12 (2143)	3.2 ± 1.05	1.96	0.589 ± 0.009	3
	Mirin (50 μM)	11 (2677)	3.3 ± 0.92	2.36	0.643 ± 0.007	2
53BP1-YFP, U2OS (G1) (100 min)	DMSO	12 (893)	3.6 ± 1.03	2.93	0.715 ± 0.011	2
	CK-689 (100 μM)	14 (926)	3.3 ± 0.89	2.41	0.709 ± 0.012	2
	CK-666 (100 μM)	14 (1234)	3.2 ± 1.03	2.32	0.669 ± 0.009	2
	Mirin (50 μM)	14 (774)	3.3 ± 1.05	2.35	0.685 ± 0.013	2
RPA32-pEGFP-NLS, MTF (100 min)	DMSO	10 (1031)	3.7 ± 1.03	3.27	0.731 ± 0.013	2
	CK-689 (100 μM)	13 (790)	4.0 ± 1.25	4.08	0.743 ± 0.012	2
	CK-666 (100 μM)	12 (823)	3.4 ± 1.01	2.07	0.66 ± 0.013	2
	Arpc2 -/- (4μM 4-OHT)	13 (1135)	3.2 ± 1.09	1.76	0.60 ± 0.011	2

b

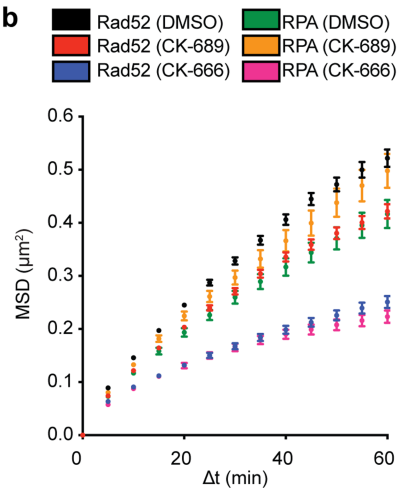

Extended Data Fig. 2 | CK-689 does not significantly alter movement of foci. a, Summary of DSB movement analyses as related to Figs. 3, 6, and Extended Data Fig. 5. **b**, MSD of RAD52–mCherry foci and RPA–pEGFP–NLS foci treated with DMSO, CK-689 and CK-666. Data shown as mean and weighted s.e.m.; RAD52: CK-689 $n = 3,262$ foci from 13 nuclei, CK-666 $n = 2,143$ foci from 12 nuclei, DMSO $n = 3,292$ foci from 12 nuclei; RPA32: CK-689 $n = 790$ foci from 13 nuclei, CK-666 $n = 823$ foci from 12 nuclei, DMSO $n = 1,031$ foci from 10 nuclei. MSD of RAD52 DMSO also shown in Fig. 6i. MSD of RAD52 CK-689 and CK-666 also shown in Fig. 3g. MSD of RPA CK-689 and CK-666 also shown in Fig. 3k.

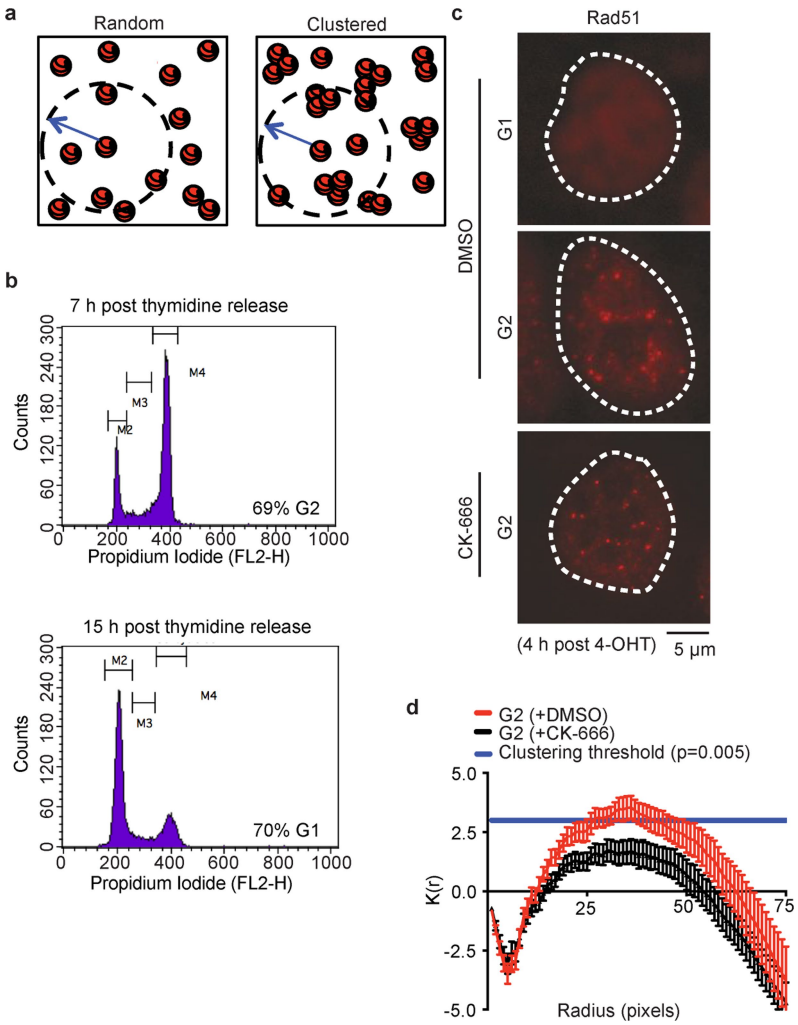

Extended Data Fig. 3 | ARP2/3 clusters RAD51 foci. a, Schematic of clustering events, as defined by the number of paired points that fall within a given radius (arrow, dashed circle). **b**, Representative cell cycle distribution of U2OS cells following double-thymidine block (out of five independent experiments). **c**, Representative images of U2OS-AsiSI nuclei showing RAD51 foci. **d**, RAD51 foci clustering in G2 cells (*P* calculated by Spatial analysis plug-in; data shown as mean and s.e.m. of Ripley function; DMSO $n = 95$ nuclei, CK-666 $n = 80$ nuclei).

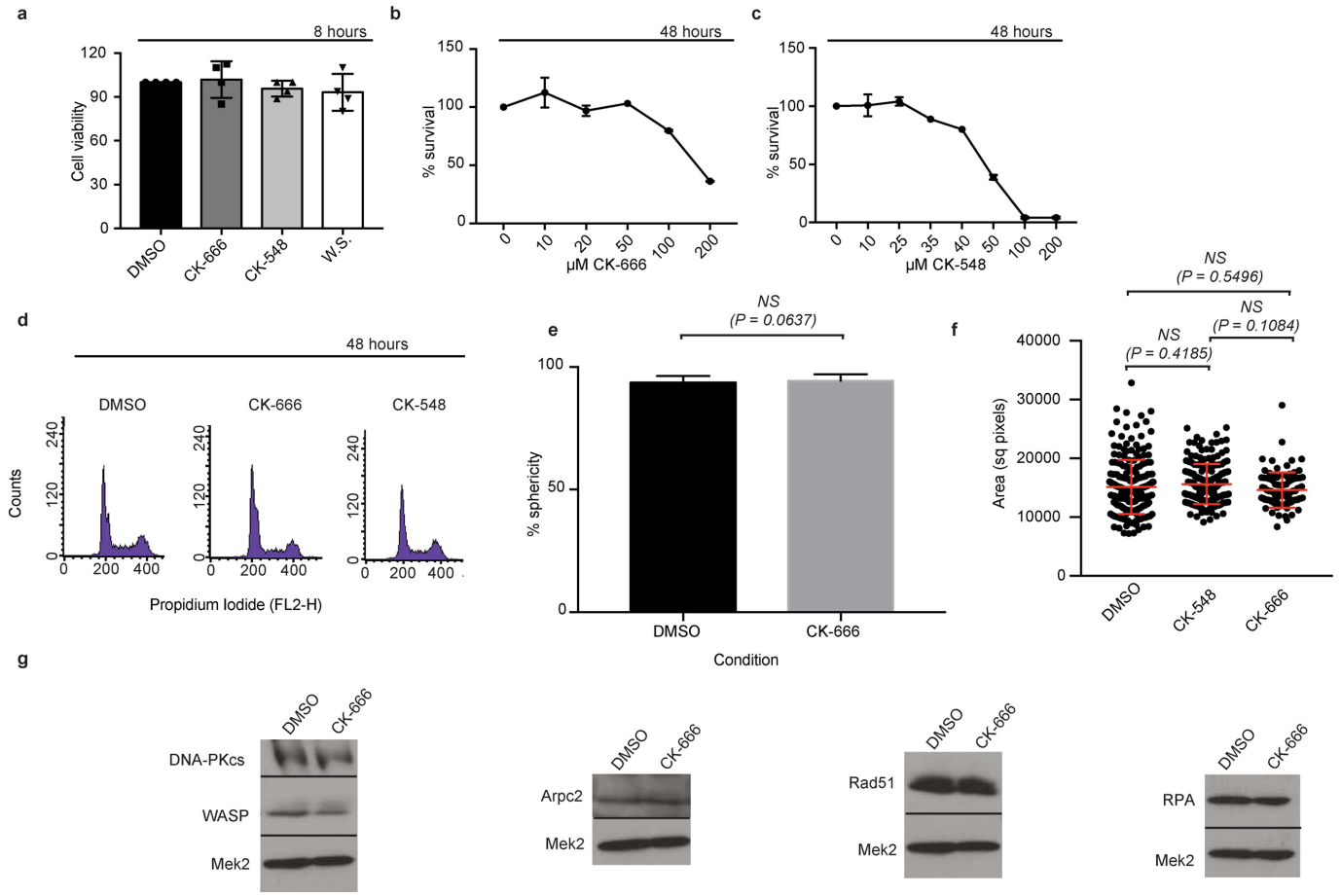

Extended Data Fig. 4 | WASP and ARP2/3 inactivation do not impair U2OS cell viability, nuclear area, nuclear sphericity or protein expression. **a**, Cell survival after 8 h of treatment with 100 μM CK-666, 50 μM CK-548, or 3 μM wiskostatin. Data shown as mean and s.e.m. $n = 4$ independent experiments. **b**, Cell survival after 48 h exposure to increasing concentrations of CK-666. $n = 3$ independent experiments. Data shown as mean and s.e.m. **c**, Cell survival after 48 h exposure to increasing concentrations of CK-548. $n = 3$ independent experiments. Data shown as mean and s.e.m. **d**, Representative cell-cycle distribution of cells treated with DMSO, 50 μM CK-666, or 25 μM CK-548 for 48 h (out of three independent experiments). **e**, Analysis of nuclear sphericity. *P* calculated by Student's two-tailed *t*-test; data shown as mean and s.d.; DMSO $n = 117$ nuclei, CK-666 $n = 117$ nuclei. NS, not significant. **f**, Analysis of nuclear area. *P* calculated by one-way ANOVA with multiple comparisons; data shown as mean and s.d.; DMSO $n = 210$ nuclei, CK-548 $n = 189$ nuclei, CK-666 $n = 92$ nuclei. **g**, Expression of RAD51, DNA-PKcs, WASP, and ARPC2 validating antibodies used in Fig. 2e–i (single experiment). MEK2 is a loading control. RPA expression levels also shown.

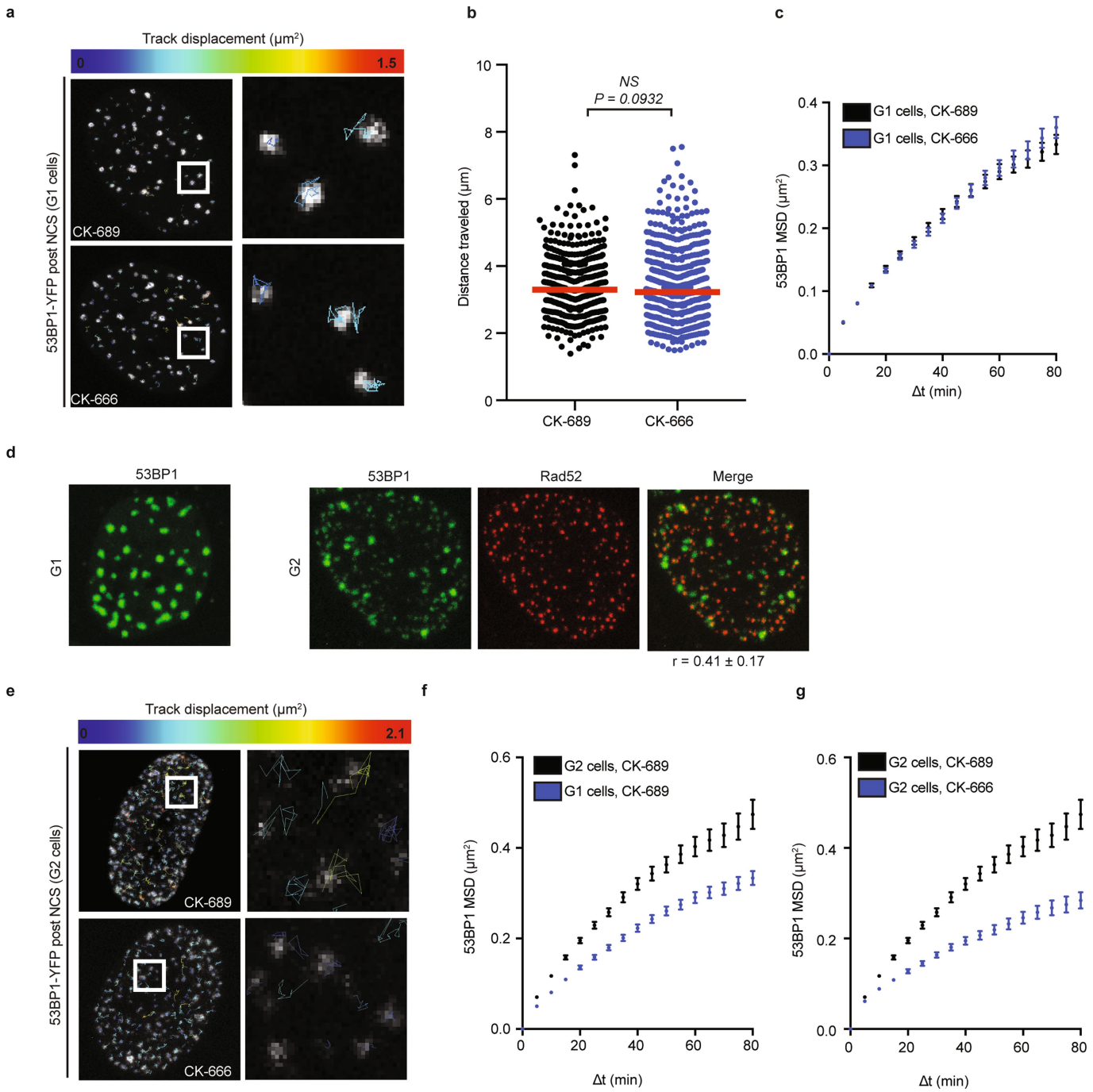

Extended Data Fig. 5 | ARP2/3 enhances movement of 53BP1 foci in G2 cells. a, Representative U2OS nuclei showing 53BP1–YFP focus traces over 100 min in G1 cells. **b**, Median cumulative distance travelled by 53BP1–YFP foci in G1 cells. *P* calculated by two-tailed Mann–Whitney test; CK-689 $n = 462$ foci from 14 nuclei, CK-666 $n = 647$ foci from 14 nuclei. NS, not significant. **c**, MSD of 53BP1–YFP foci in G1 cells. Data shown as mean and weighted s.e.m.; CK-689 $n = 926$ foci from 14 nuclei, CK-666 $n = 1{,}234$ foci from 14 nuclei. Δt, time interval. **d**, Left, a representative G1 cell with 53BP1–YFP foci. Right, a representative G2 cell with 53BP1–YFP and Rad52–mCherry foci. 53BP1 foci colocalize with RAD52 foci. $r = 0.41 \pm 0.17$, Pearson, $n = 5$ independent experiments. **e**, Representative U2OS nuclei showing traces of 53BP1–YFP foci over 100 min in G2 cells. **f**, MSD of 53BP1–YFP foci. Data shown as mean and weighted s.e.m.; G1 CK-689 $n = 926$ foci from 14 nuclei, G2 CK-689 $n = 1{,}403$ foci from 12 nuclei. G1 CK-689 curve also shown in **c**. **g**, MSD of 53BP1–YFP foci in G2 cells. Data shown as mean and weighted s.e.m.; CK-689 $n = 1{,}403$ foci from 12 nuclei, CK-666 $n = 1{,}038$ foci from 10 nuclei. G2 CK-689 curve also shown in **f**.

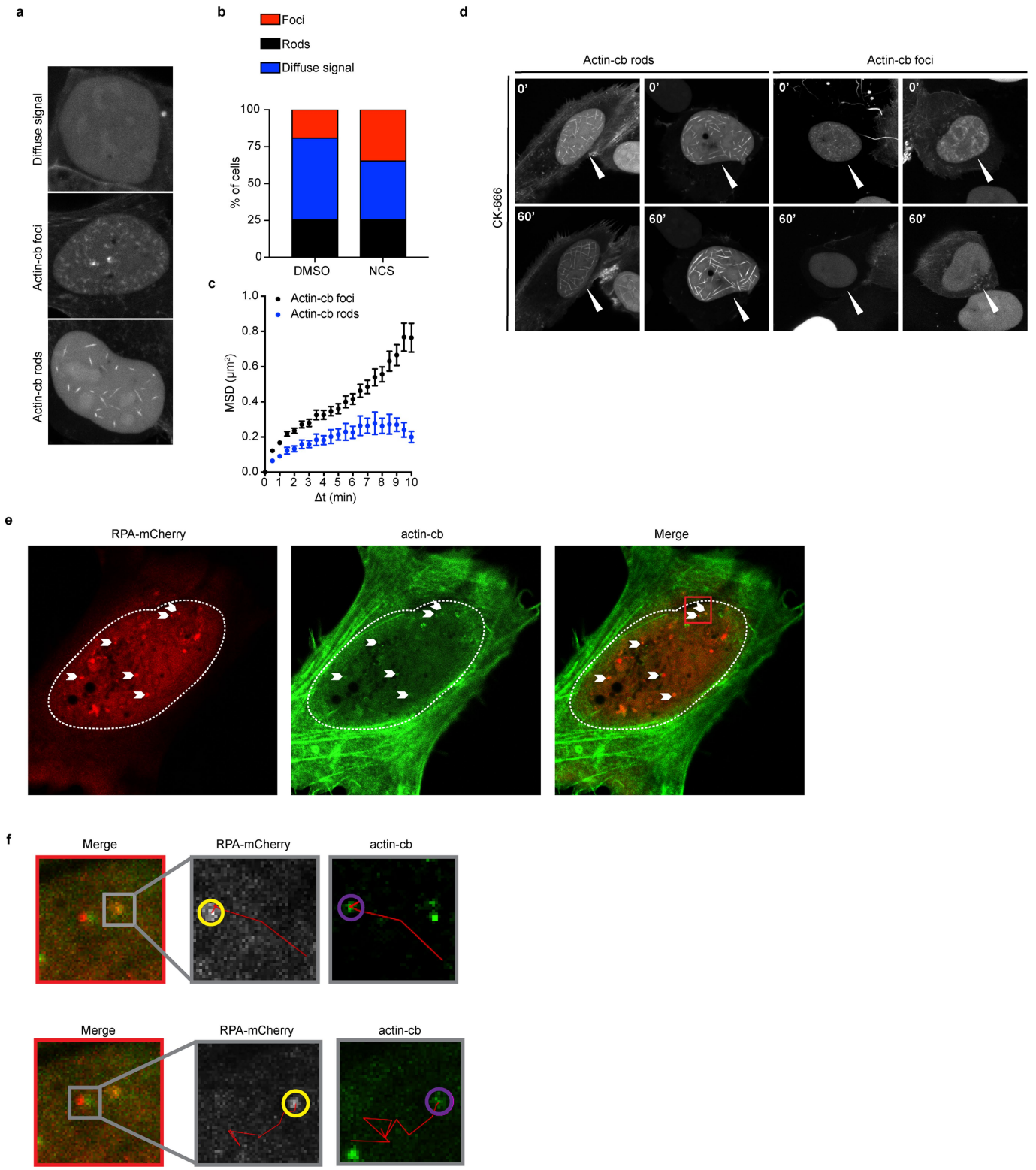

Extended Data Fig. 6 | ARP2/3 promotes assembly of actin foci following DNA damage. a, Representative U2OS nuclei showing classes of nuclear actin structures following transient transfection with nuclear actin-chromobody TagGFP. **b**, Percentage of cells with diffuse signal, nuclear actin-cb foci, or rods with or without NCS (DMSO $n = 473$ cells, NCS $n = 473$ cells). **c**, MSD of actin-cb foci and actin-cb rods. Data shown as mean and weighted s.e.m.; actin-cb foci $n = 662$ foci from 11 nuclei, actin-cb rods $n = 161$ rods from 5 nuclei. **d**, Representative images of U2OS nuclei with actin rods or actin-cb foci following CK-666 treatment ($n = 5$ independent experiments). **e**, Representative image of a U2OS nucleus with RPA–mCherry and actin-cb foci of $n = 3$ independent experiments. Arrowheads indicate sites of RPA–mCherry and actin-cb co-localization. **f**, Expanded image of RPA–mCherry and actin-cb co-localization from **e** (red box). Traces of RPA and actin-cb foci are shown in red. Yellow and purple circles encompass RPA and actin-cb foci, respectively. $n = 3$ independent experiments.

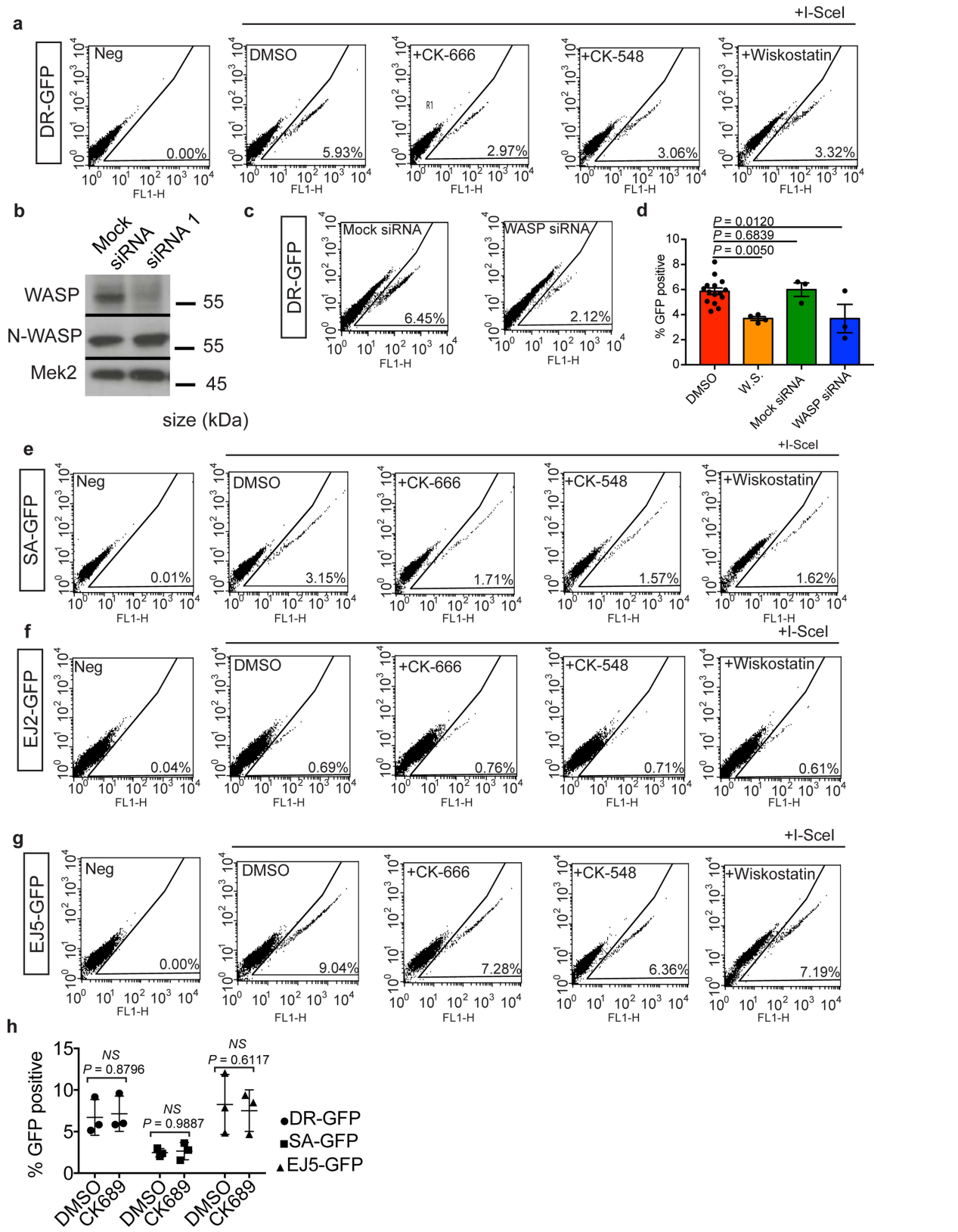

Extended Data Fig. 7 | WASP and ARP2/3 mediate DSB repair by homology-directed mechanisms a, Representative FACS plots of GFP$^+$ cells in the HDR (DR-GFP) assay. **b**, Western blot shows expression of WASP and N-WASP following WASP siRNA knockdown in whole-cell lysates (single experiment). WASP siRNA 1: 5′-GAGUGGCUGAGUUACUUGC-3′. **c**, Representative FACS plots of GFP$^+$ cells in the HDR (DR-GFP) assay in WASP and mock-depleted cells. **d**, Summary of DR-GFP assay with WASP depletion. *P* calculated by one-way ANOVA with multiple comparisons; data shown as mean and s.e.m; $n = 3$ independent experiments. HDR efficiency in the presence of DMSO or wiskostatin (Fig. 5a) shown for comparison. **e**, Representative FACS plots of GFP$^+$ cells in the SSA (SA-GFP) assay. **f**, Representative FACS plots of GFP$^+$ cells in the MMEJ (EJ2-GFP) assay. **g**, Representative FACS plots of GFP$^+$ cells in the NHEJ (EJ5-GFP) assay. **h**, Summary of DR-GFP, SA-GFP, and EJ5-GFP assays with CK-689. *P* calculated by two-way ANOVA with multiple comparisons; data shown as mean and s.d.; $n = 3$ independent experiments. NS, not significant.

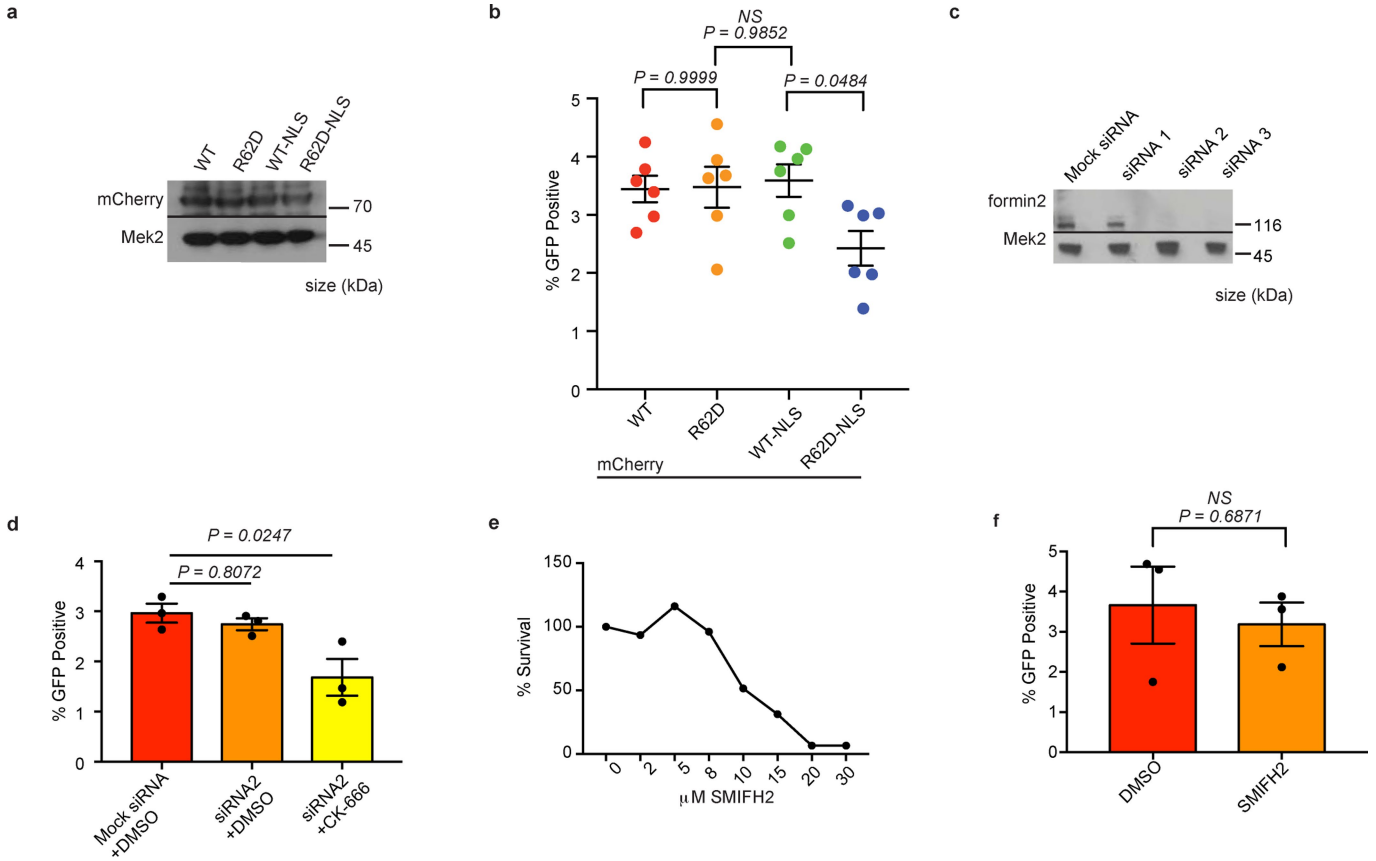

Extended Data Fig. 8 | Actin nucleation regulates HDR in the nucleus and does not require formin-2 activity. a, Western blot shows expression of mCherry-tagged actin constructs in U2OS whole-cell lysates (single experiment). **b**, Summary of DR-GFP (HDR) assay. *P* calculated by one-way ANOVA with multiple comparisons; data shown as mean and s.e.m; $n = 6$ independent experiments. **c**, Western blot shows knockdown of formin-2 following 48 h transfection of mock or sequence-specific siRNA oligos (single experiment). Formin-2 siRNA #2: 5′-CGUGUAAUCAGAAUGCCCA-3′. **d**, Summary of DR-GFP assay. *P* calculated by one-way ANOVA with multiple comparisons; data shown as mean and s.e.m; $n = 3$ independent experiments. **e**, Mean cell survival after 48 h exposure to increasing concentrations of the formin inhibitor SMIFH2 ($n = 3$ independent experiments). **f**, Summary of DR-GFP assay. *P* calculated by Student's two-tailed *t*-test; data shown as mean and s.e.m; $n = 3$ independent experiments.

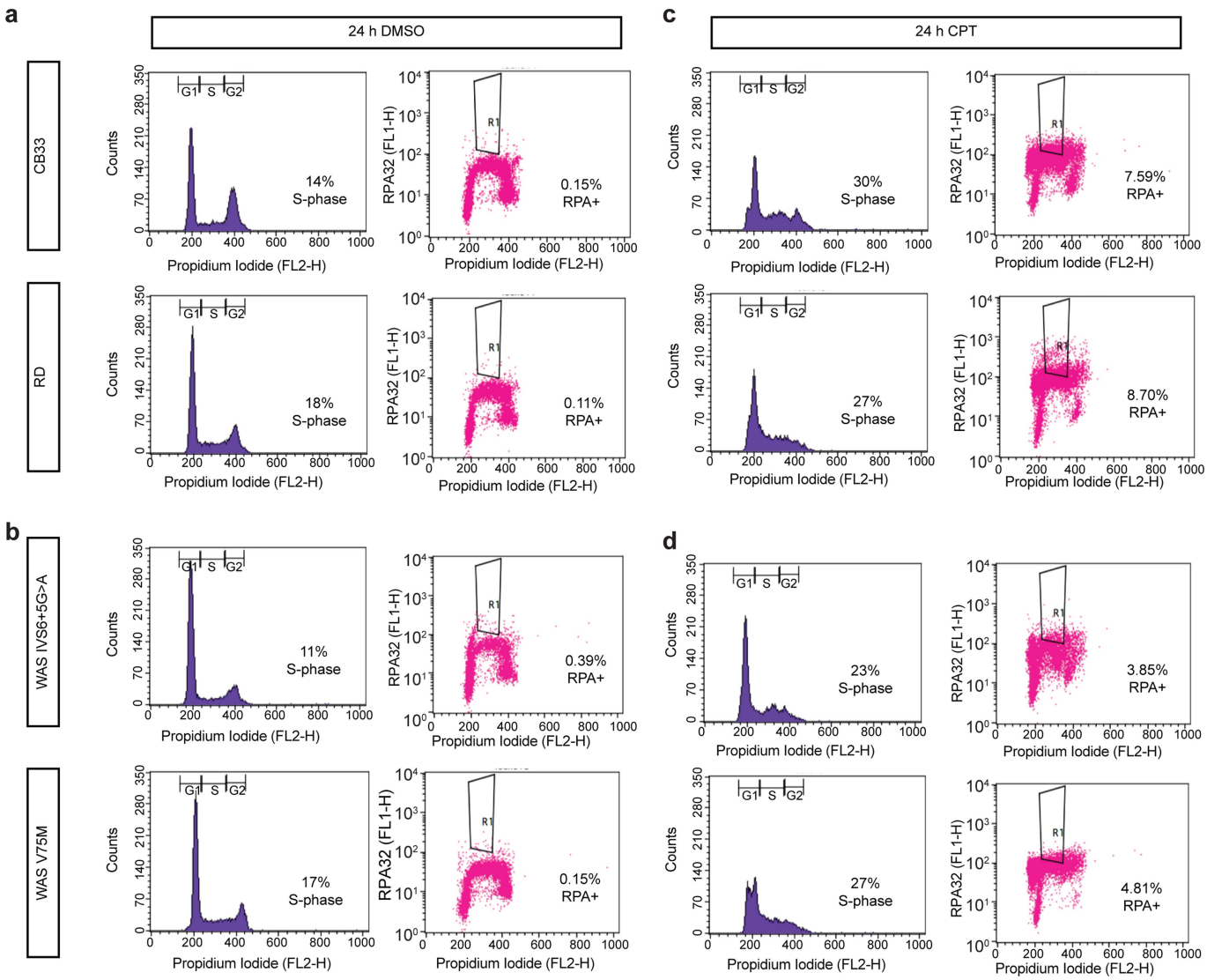

Extended Data Fig. 9 | B lymphocytes derived from patients with WAS exhibit reduced DSB end-resection. a, Representative cell cycle distribution of CB33 and RD lymphocytes derived from healthy individuals following DMSO treatment (left). The percentage of RPA-positive S-phase cells following DMSO treatment was measured by flow cytometry (right). **b**, Representative cell cycle distribution of lymphocytes bearing the V75M mutation in the *WAS* gene or a G>A transition at position 5 in intron 6 of the *WAS* gene (IVS6+5G>A) following DMSO treatment (left). The percentage of RPA-positive S-phase cells following DMSO treatment was measured by flow cytometry (right). **c**, Representative cell cycle distribution of CB33 and RD lymphocytes following CPT treatment (left). The percentage of RPA-positive S-phase cells following CPT treatment was measured by flow cytometry (right). **d**, The cell cycle distribution of *WAS* V75M or *WAS* IVS6+5G>A lymphocytes following CPT treatment (left). The percentage of RPA-positive S-phase cells following CPT treatment was measured by flow cytometry (right). For all panels, $n = 4$ independent experiments.

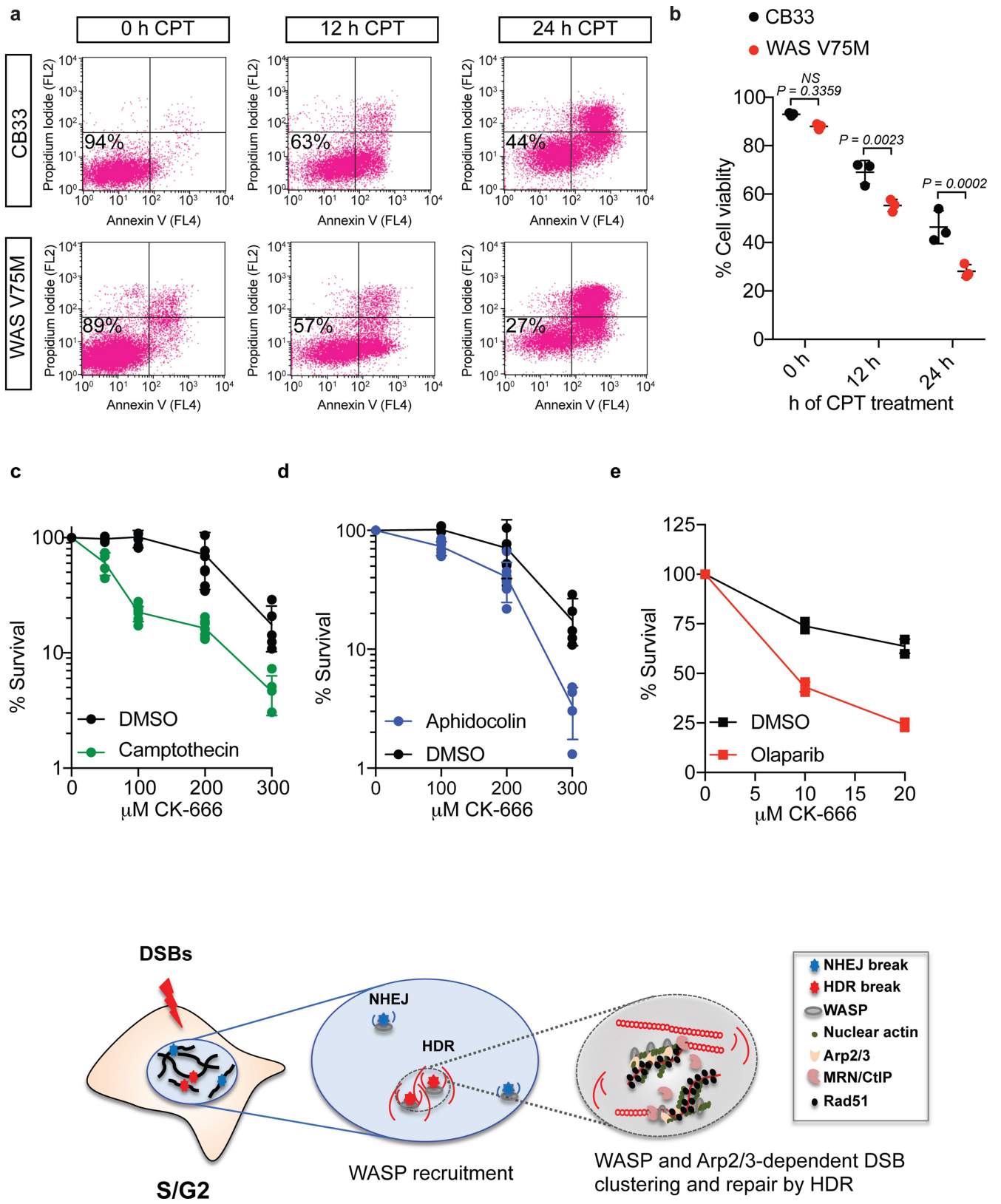

Extended Data Fig. 10 | See next page for caption.

Extended Data Fig. 10 | ARP2/3 inactivation confers sensitivity to DSBs induced in S-phase as well as replication-stress-inducing agents. **a**, Control CB33 lymphocytes or lymphocytes bearing a V75M mutation in the *WAS* gene were treated with CPT for 0, 12, or 24 h. Per cent viability following CPT treatment was assessed by measuring the fraction of annexin V- and PI-negative cells by flow cytometry. **b**, Summary of CB33 or *WAS* V75M lymphocyte survival following CPT treatment. *P* calculated by two-way ANOVA with multiple comparisons; data shown as mean and s.d.; $n = 3$ independent experiments. **c**, Clonogenic U2OS cell survival after 12 h of CPT treatment in the presence of DMSO or increasing concentrations of CK-666. Triplicate experiments; data shown as mean and s.d.; $n = 2$ independent experiments. **d**, Clonogenic U2OS cell survival after 12 h of aphidicolin treatment in the presence of DMSO or increasing concentrations of CK-666. Triplicate experiments; data shown as mean and s.d.; $n = 2$ independent experiments. **e**, Clonogenic U2OS cell survival after olaparib treatment in the presence of DMSO or increasing concentrations of CK-666 for 14 days. Triplicate experiments; data shown as mean and s.e.m.; $n = 2$ independent experiments. **f**, DNA damage induces DSBs, which are repaired preferentially by NHEJ in mammalian cells (blue). In S/G2, DSBs may be repaired by HDR (red). All DSBs recruit WASP, but ARP2/3-dependent actin polymerization occurs only at HDR breaks, which become more mobile. Actin polymerization in the vicinity of DSBs generates forces that result in DSB clustering, optimal DNA end resection, formation of RAD51 foci, and HDR.

nature research

Corresponding Author: Jean Gautier

Date: 4/04/2018

Life Sciences Reporting Summary

Nature Research wishes to improve the reproducibility of the work we publish. This form is published with all life science papers and is intended to promote consistency and transparency in reporting. All life sciences submissions use this form; while some list items might not apply to an individual manuscript, all fields must be completed for clarity.

For further information on the points included in this form, see Reporting Life Sciences Research. For further information on Nature Research policies, including our data availability policy, see Authors & Referees and the Editorial Policy Checklist.

Experimental design

1. Sample size

   Describe how sample size was determined.

   We did not compute statistical analyses to predetermine sample sizes prior to performing experiments. However, our sample sizes are similar to those published elsewhere. We describe sample sizes in greater detail in the Methods section of the paper.

2. Data exclusions

   Describe any data exclusions.

   a. For chromatin binding assays, we interpreted successful experiments using the following three pre-established conditions; first, no contamination of proteins in the no sperm control; second, greater than two-fold induction of RPA in extracts supplemented with chromatin and PFLM1 relative to extracts supplemented with DMSO; and third, equal chromatin loading between samples, as measured by total Histone H3.
   b. For experiments monitoring DSB foci by immunofluorescence, we interpreted successful IF techniques by evaluating greater than ~ten-fold more foci in cells treated with DNA damaging agents relative to cells treated with DMSO.
   c. Live Cell Imaging: Cells that migrated outside the field of view during recording were discarded. Cells with nuclear membrane perturbation during recording were discarded.
   d. GFP Reporter assays: For the DR-GFP assay, we interpreted successful experiments by measuring more than 3% GFP+ cells in cells treated with I-SCEI.

3. Replication

   Describe whether the experimental findings were reliably reproduced.

   Each experiment was repeated at least twice to confirm reproducibility of findings.

4. Randomization

   Describe how samples/organisms/participants were allocated into experimental groups.

   Cell cultures are not subjected to randomization. When preparing cell-free extracts from Xenopus eggs, the organisms (Xenopus females) are not allocated into experimental groups. We prepare extracts from the eggs of several females (3-4 females in a typical experiment). The eggs are combined before extract preparation. The cell-free extract is either used on the day of preparation or can be aliquoted and frozen for subsequent use.

5. Blinding

   Describe whether the investigators were blinded to group allocation during data collection and/or analysis.

   Data collection (foci counts, FACS, foci mean square displacement analysis) was not blinded and instead acquired through automated software, as detailed in the methods section.

Note: all studies involving animals and/or human research participants must disclose whether blinding and randomization were used.

6. Statistical parameters

For all figures and tables that use statistical methods, confirm that the following items are present in relevant figure legends (or the Methods section if additional space is needed).

n/a	Confirmed
☐	☒ The exact sample size (*n*) for each experimental group/condition, given as a discrete number and unit of measurement (animals, litters, cultures, etc.)
☐	☒ A description of how samples were collected, noting whether measurements were taken from distinct samples or whether the same sample was measured repeatedly.
☐	☒ A statement indicating how many times each experiment was replicated
☐	☒ The statistical test(s) used and whether they are one- or two-sided (note: only common tests should be described solely by name; more complex techniques should be described in the Methods section)
☐	☒ A description of any assumptions or corrections, such as an adjustment for multiple comparisons
☐	☒ The test results (e.g. *p* values) given as exact values whenever possible and with confidence intervals noted
☐	☒ A summary of the descriptive statistics, including central tendency (e.g. median, mean) and variation (e.g. standard deviation, interquartile range)
☐	☒ Clearly defined error bars

See the web collection on statistics for biologists for further resources and guidance.

Software

Policy information about availability of computer code

7. Software

Describe the software used to analyze the data in this study.

a. MetaCyte software (Version 3.10.6, Metasystems, Newton, MA, USA)
b. Icy Software (Version 1.8.6.0; Institut Pasteur, Quantitative Image Analysis Unit; http://www.icy.bioimageanalysis.org).
c. ImageJ (Version 2.0.0-rc-59/1.51n; StackReg and TrackMate plug-ins)
d. Matlab (Version 2017A; @msdanalyzer)
e. Prism (Version 7.9)
f. Proteome Discoverer software (Thermo, Version 1.4).

For all studies, we encourage code deposition in a community repository (e.g. GitHub). Authors must make computer code available to editors and reviewers upon request. The *Nature Methods* guidance for providing algorithms and software for publication may be useful for any submission.

Materials and reagents

Policy information about availability of materials

8. Materials availability

Indicate whether there are restrictions on availability of unique materials or if these materials are only available for distribution by a for-profit company.

No restrictions

9. Antibodies

Describe the antibodies used and how they were validated for use in the system under study (i.e. assay and species).

1. Arpc2 (p34-arc); Usage: ChIP (10 µg) , WB (1:500); Vendor: Santa Cruz Biotechnology, Inc.; Cat#sc-32195; RRID: C1213. Validated for WB by manufacturer. Validated for ChIP by Taylor et al., 2010.
2. Rad51; Usage: ChIP (10 µg), IHC (1:50), WB (1:500); Vendor: Santa Cruz Biotechnology, Inc.; Cat#sc-8349; RRID: J0215. Validated for WB and IHC by manufacturer. Validated for ChIP by Aymard et al., 2014.
3. Beta-actin; Usage: WB (1:5000); Vendor: Sigma Aldrich Cat#A5316; RRID: 095M4811V. Validated for WB by manufacturer.
4. WASP; Usage: ChIP (10 µg), IHC (1:50), WB (1:500); Vendor: Santa Cruz Biotechnology, Inc.; Cat#sc-5300; RRID: H1913. Validated for WB and IHC by manufacturer. Validated for ChIP by Taylor et al., 2010.
5. DNA-PKcs; Usage: ChIP (10 µg), WB (1:500); Vendor: Abcam; Cat#ab1832; RRID: GR261379-2. Validated for WB by manufacturer. Validated for ChIP by Zhou et al., 2013.
6. Arpc4; Usage: WB (1:500); Vendor: Novus Biologicals; Cat#NBP1-69003; RRID: QC2587-41600. Validated for WB by manufacturer.
7. Alexa 488 conjugated goat anti-mouse IgG; Usage: IHC (1:1000); Vendor: Abcam; Cat#ab150113. Validated for IHC by manufacturer.
8. Alexa 488 conjugated goat anti-rabbit IgG; Usage: IHC (1:1000); Vendor: Thermo Fisher Scientific; Cat#A-11034. Validated for IHC by manufacturer.
9. Alexa 594 conjugated goat anti-mouse IgG; Usage: IHC (1:1000); Vendor: Thermo Fisher Scientific; Cat#A-11005. Validated for IHC by manufacturer.
10. Formin 2; Usage: WB (1:500); Vendor: Novus Biologicals; Cat#H00056776-A01; RRID: 08226. Validated for WB by manufacturer.
11. Capping protein beta-2 subunit; Usage: WB (1:5000); Vendor: Developmental Studies Hybridoma Bank; Cat#E00007. Validated for WB by manufacturer.
12. N-WASp; Usage: WB (1:500); Vendor: Abcam; Cat#Ab187527; RRID: GR235374-8. Validated for WB by manufacturer.
13. Histone H3; Usage: WB (1:2000); Vendor: Cell Signaling Technology; Cat#9715; RRID: 20. Validated for WB by manufacturer.
14. mCherry; Usage: WB (1:500); Vendor: Novus Biologicals; Cat# NBP2-25157SS. Validated for WB by manufacturer.
15. RPA32/RPA2, Usage: WB (1:500), flow cytometry (1:50); Vendor: Abcam; Cat#ab2175. Validated for WB, IHC, and flow cytometry by manufacturer.
16. Alexa 647 conjugated donkey anti-mouse Ig, Usage: flow cytometry (1:50); Vendor: Invitrogen: A31571. Validated for flow cytometry by manufacturer.

10. Eukaryotic cell lines

a. State the source of each eukaryotic cell line used.

1. Human: ER-AsiSI U2OS cell line; Laboratory of Dr. Gaelle Legube (Aymard et al., 2014)
2. Human: ER-AsiSI-AID U2OS cell line; Laboratory of Dr. Gaelle Legube (Aymard et al., 2014)
3. Human: DR-GFP U2OS cell line; Laboratory of Dr. Jeremy Stark (Gunn and Stark, 2012)
4. Human: SA-GFP U2OS cell line; Laboratory of Dr. Jeremy Stark (Gunn and Stark, 2012)
5. Human: EJ5-GFP U2OS cell line; Laboratory of Dr. Jeremy Stark (Gunn and Stark, 2012)
6. Human: EJ2-GFP U2OS cell line; Laboratory of Dr. Jeremy Stark (Gunn and Stark, 2012)
7. Human: 53BP1-YFP, Rad52-mCherry U2OS cell line; Laboratory of Dr. Galit Lahav (Karanam et al., 2012)
8. Mouse: Mouse embryonic fibroblasts; ICRC
9. Mouse: Arpc2 CreER mouse tail fibroblasts; Laboratory of Dr. James Bear (Rotty et al., 2015)
10. Human CB33 B-lymphocyte cell line; Laboratory of Dr. Riccardo Dalla-Favera (Columbia University).
11. Human RD B-lymphocyte cell line; Laboratory of Dr. Riccardo Dalla-Favera (Columbia University).
12. WAS B-lymphocyte cell line harboring G>A transition at position 4 in intron 6 of the WAS gene (IVS6+5G>A); NIGMS Human Genetic Cell Repository (Coriell: GM1267).
13. WAS B-lymphocyte cell line harboring a G>A transition at nucleotide 257 in exon 2 of the WAS Gene (V75M): NIGMS Human Genetic Cell Repository (Coriell: GM1268).

b. Describe the method of cell line authentication used.

Cell lines have not been authenticated.

c. Report whether the cell lines were tested for mycoplasma contamination.

Cell lines have tested negative for mycoplasma contamination.

d. If any of the cell lines used in the paper are listed in the database of commonly misidentified cell lines maintained by ICLAC, provide a scientific rationale for their use.

None of the cell lines used in the paper are listed in the ICLAC database.

Animals and human research participants

Policy information about studies involving animals; when reporting animal research, follow the ARRIVE guidelines

11. Description of research animals

Provide details on animals and/or animal-derived materials used in the study.

The animals are adult (one-year-old) Xenopus laevis females. Upon arrival at the ICRC 6th floor facility, the animals are kept in quarantine for 2 weeks in a separate tank to avoid possible contamination of the rest of the animals. Each month, for ten months of the year, 10 animals are injected with HCG. The animals are injected the evening prior to the experiments. The animals are kept in small individual tanks until the morning when the eggs are collected. The eggs are collected throughout the day. At the end of the day, the females are returned into the large tanks of the aquatic facility.

Policy information about studies involving human research participants

12. Description of human research participants

Describe the covariate-relevant population characteristics of the human research participants.

The study did not involve human research participants.

nature research

Corresponding author(s): Jean Gautier

☐ Initial submission ☐ Revised version ☒ Final submission

Flow Cytometry Reporting Summary

Form fields will expand as needed. Please do not leave fields blank.

Data presentation

For all flow cytometry data, confirm that:

☒ 1. The axis labels state the marker and fluorochrome used (e.g. CD4-FITC).

☒ 2. The axis scales are clearly visible. Include numbers along axes only for bottom left plot of group (a 'group' is an analysis of identical markers).

☒ 3. All plots are contour plots with outliers or pseudocolor plots.

☒ 4. A numerical value for number of cells or percentage (with statistics) is provided.

Methodological details

5. Describe the sample preparation.	U2OS cells are trypsinized and washed with PBS.
6. Identify the instrument used for data collection.	BD FACSCALIBUR
7. Describe the software used to collect and analyze the flow cytometry data.	CellQuest Pro was used to collect and analyze the data.
8. Describe the abundance of the relevant cell populations within post-sort fractions.	10,000 cells were collected for each biological replicate.
9. Describe the gating strategy used.	For the GFP reporter assays, gating for GFP+ cells was established by selecting the population of GFP+ cells that express the pEGFP plasmid. The same gate was used for all subsequent studies. For experiments that quantify RPA association to chromatin by flow cytometry: The percentage of S-phase cells as identified by PI staining was quantified by flow cytometry. The gate for RPA-positive cells was established using a negative control sample that was stained with mouse IgG following extraction. RPA-positive cells following DMSO and CPT treatment were subsequently quantified by flow cytometry. For Annexin V/propidium iodide survival assays, % viability following camptothecin treatment was assessed by measuring the percentage of APC-Annexin V-negative and propidium iodide-negative cells by flow cytometry.

Tick this box to confirm that a figure exemplifying the gating strategy is provided in the Supplementary Information. ☒